Helmholtz-Zentrum Geesthacht
Zentrum für Material- und Küstenforschung

MONTAN UNIVERSITÄT
WWW.UNILEOBEN.AC.AT

Carbide precipitates in as-sintered and heat treated Ti-22Nb-(10Zr-xB) alloys processed by metal injection molding

Diploma Thesis

Sandra Ebner

This thesis was carried out at the Department of Physical Metallurgy and Materials Testing at the Montanuniversität Leoben in cooperation with the Department of Materials Design and Characterization at the Helmholtz-Zentrum Geesthacht.

Leoben, June 2016

Affidavit

I declare in lieu of oath that I wrote this thesis and performed the associated research myself, using only literature cited in this volume.

Eidesstattliche Erklärung

Ich erkläre an Eides statt, dass ich diese Arbeit selbstständig verfasst, andere als die angegebenen Quellen und Hilfsmittel nicht benutzt und mich auch sonst keiner unerlaubten Hilfsmittel bedient habe.

Leoben, Juni 2016 Sandra Ebner

Acknowledgments

First of all, I want to thank Univ.-Prof. Dipl.-Ing. Dr.mont. Helmut Clemens and Prof. Dr. Regine Willumeit-Römer for providing me the opportunity to write my thesis at the Helmholtz-Zentrum Geesthacht.

My sincere thanks and appreciation go to my supervisor Dr. Thomas Ebel for supporting me throughout my work. His office was always open for anything that has crossed my mind.

Furthermore, I would like to thank all my colleagues from the Department of Materials Design and Characterization at the Helmholtz-Zentrum Geesthacht for providing me with such a good working environment. Especially, I want to thank Ms. Alexandra Amherd Hidalgo, Mr. Johannes Schaper and Mr. Wolfgang Limberg for their help and suggestions in needful moments.

I am greatly thankful for the technical and scientific support of Mrs. Petra Fischer, Mr. Uwe Lorenz, Dr. Michael Oehring and Dr.rer.nat. Daniel Höche. Their knowledge was very valuable for my work.

Sincere thanks to all my friends for the great time in Leoben. You always had an open ear for my problems and you made life more enjoyable. Thank you for all the amazing memories that I will never forget.

My special acknowledgments to Mr. Andreas Jamnig for the time and patience he spent on our learning sessions. We nearly brought the “How-to-study-efficiently-with-limited-time” to perfection.

My studies would have been impossible without my family who supported and encouraged me in every aspect of my life. Thank you so much for everything!

Finally, I would like to thank Lukas for his love and friendship in the last years.

Content

Abbreviations

bcc	body-centered cubic
BSE	backscattered electrons
CP	commercially pure
DSC	differential scanning calorimetry
EBSD	electron backscatter diffraction
EDS	energy-dispersive spectroscopy
fcc	face-centered cubic
hcp	hexagonal closed-packed
m.%	percentage by mass
MIM	metal injection molding
M_s	martensitic start temperature
RT	room temperature
SE	secondary electrons
SEM	scanning electron microscope/microscopy
TEM	transmission electron microscope/microscopy
XRD	X-ray diffraction
α	alpha phase, titanium
β	beta phase, titanium

1 Introduction

The continuous progress in the development of biocompatible materials for medical applications reflects the increasing number of people who are dependent on partial or complete tissue replacement. Currently, the majority of implants are made of metals and metal alloys including stainless steel, CrCo-based alloys or Ti and Ti-alloys [1]. They are mainly applied as hard tissue implants (e.g. artificial hip or knee joints) or as fixation and stabilization elements (screws, stents and wires) [2].

Among the metallic biomaterials available for biomedical applications, Ti and Ti-alloys are the most attractive choice thanks to their excellent combination of properties. They exhibit low Young's modulus, high strength-to-weight ratio, good corrosion resistance and outstanding biocompatibility [3]. Until now, commercially pure titanium (CP-Ti) and Ti-6Al-4V are the most commonly used Ti and Ti-alloys in the biomedical sector. The most recent development of β-Ti alloys (e.g. Ti-Nb alloys) complies with the demand of enhancing biocompatibility and decreasing the Young's modulus. The latter is especially important to avoid the so-called stress-shielding effect, which occurs if the mismatch between the Young's modulus of bone and implant is too high. This can lead to the degeneration of bone cells around the implant and, consequently, to bone resorption and implant loosening. In fact, β-titanium alloys exhibit a Young's modulus of 50-60 GPa, which is much closer to that of human cortical bone (10-40 GPa) than the Young's modulus of α- or (α+β)-titanium alloys (∼100 GPa) [4].

However, the traditional processing techniques limit the applications of titanium and titanium alloys due to the rather high costs of raw material and machining and the constraints in design flexibility. Metal injection molding (MIM) presents a promising alternative to overcome these limitations. MIM is a near-net-shape technique that allows the economic production of complex parts in high numbers. Nowadays, it is possible to fabricate titanium products by MIM with properties similar to those of wrought materials. Consequently, some permanent implants made by MIM are already available on the market [5].

As a drawback, the fabrication of Ti-Nb alloys using the MIM route turned out to lead to the formation of titanium carbides at grain boundaries, which adversely affects the mechanical properties, especially the ductility [6]. Several efforts have been made to reduce these carbide precipitates. Previous research found that the addition of zirconium or boron to Ti-Nb alloys leads to carbide reduction [7, 8]. Furthermore, it is stated that proper heat treatments are also suitable to decrease the amount of titanium carbides [6]. However, much uncertainty still exists in both studies and the mechanisms behind are unclear. Thus,

further investigations on the potential of heat treatments concerning carbide reduction in Ti-Nb alloys are necessary, being the goal of this work.

2 Scope of this work

In the present work, different compositions of Ti-22Nb-(10Zr-xB) alloys with x=0, 0.3 and 0.5 (all m.%) were prepared, consolidated by metal injection molding, and subsequently heat treated. Zirconium and boron are chosen with regard to the previous works of Beißig [8] and Nagaram [7]. They affirmed that the addition of these elements is beneficial for carbide reduction. The selection of the heat treatments performed in this study is based on the Ti-22Nb – C phase diagram calculated within the work of Zhao [6] (see chapter 3.3.1, p.12).
The evolution of the microstructure, particularly the precipitation of titanium carbides, in the as-sintered and heat treated condition is studied using optical and scanning electron microscopy (SEM). Grain size, porosity and the amount of precipitates were determined. Elemental composition was assessed by energy-dispersive spectroscopy (EDS). Furthermore, differential scanning calorimetry (DSC) and X-ray diffraction (XRD) were performed to study phase transformations.
Finally, the influence of zirconium and boron addition to Ti-22Nb is analyzed and the effect of different heat treatments on the microstructure is discussed.

3 State of the art

3.1 Ti and Ti-alloys

Titanium is with a level of 0.6% one of the most plentiful elements in the earth's crust and the fourth most abundant structural metal after aluminum, iron and magnesium. It has some outstanding properties such as low density, high strength and good corrosion resistance, and is therefore used in various fields. The main areas of applications for titanium can be found in aerospace and automotive industry, chemical industry and in the biomedical sector [9].
Titanium has a melting point of 1670 °C and occurs in different crystal structures. At ambient temperature and pressure Ti and most Ti-alloys crystallize in a hexagonal closed-packed (hcp) crystal structure (α phase). At higher temperature Ti transforms into a body-centered cubic (bcc) crystal structure (β phase). The allotropic temperature varies with alloying elements and for pure Ti it is 882±2 °C. Figure 3.1 shows the unit cell of hcp α phase (left) and bcc β phase (right) with their respective most densely packed lattice planes. The lattice parameters for α at room temperature and for β at 900 °C are also indicated. Due to the hexagonal crystal structure, α has anisotropic mechanical and physical properties. Compared to β, α shows reduced ductility, higher resistance to plastic deformation, higher creep resistance and a lower diffusion rate [10].

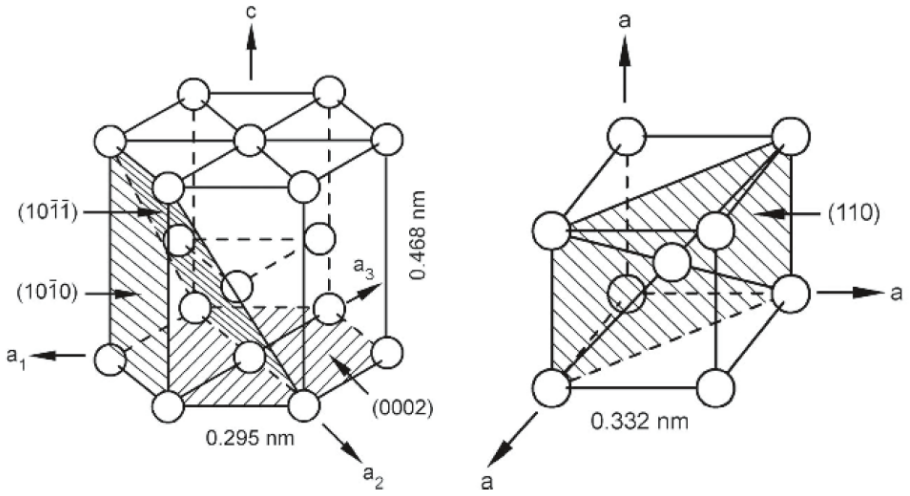

Figure 3.1: Unit cell of α titanium (left) and β titanium (right) [9]

The phase transformation from the β phase to α phase is a diffusion controlled nucleation and growth process. The Burgers relationship between α and β is given as

$$(110)_\beta \,||\, (0002)_\alpha$$
$$[1\bar{1}1]_\beta \,||\, [11\bar{2}0]_\alpha.$$

According to this relationship, the 12 slip systems of β (six slip planes and two slip directions) give a maximum of 12 variants of orientation for α. Alpha nucleates preferentially at grain boundaries and grows into the grain as parallel plates that belong to the same variation of the Burgers relationship. The so formed alpha colonies result in a lamellar microstructure, also called basket weave structure. Besides, there is also the possibility of martensitic transformation. Two martensitic structures are observed in titanium and titanium alloys: the hexagonal α' and the orthorhombic α''. The martensitic start temperature (M_s) as well as the α'/α'' boundary depend on the content of impurities and alloying elements. In general, an increase in β-stabilizing elements decreases M_s and favors the formation of α''. There is also another phase, the ω phase, which has no practical application and is usually not desired [9].

Titanium materials are mainly used as alloys. With respect to their effect on the beta transus temperature, the alloying elements can be divided in three different groups: α stabilizers (Al, O, N, C, B), β stabilizers (isomorphous: V, Mo, Nb, Ta; eutectoid: Fe, Mn, Cr, Ni, Cu, Si, H) and neutral elements (Sn) [10]. The effect of zirconium is not clear. Zirconium is either counted as neutral [10] or as additional β stabilizer in combination with other beta-stabilizing elements [11].
Based on the amount of beta stabilizers, Ti-alloys are classified in α, α+β and β alloys with further subdivision into near-α and metastable-β alloys. This alloy classification is illustrated in Figure 3.2. The properties of titanium alloys are characterized by the volume fraction, arrangement and individual properties of α and β phase [10].

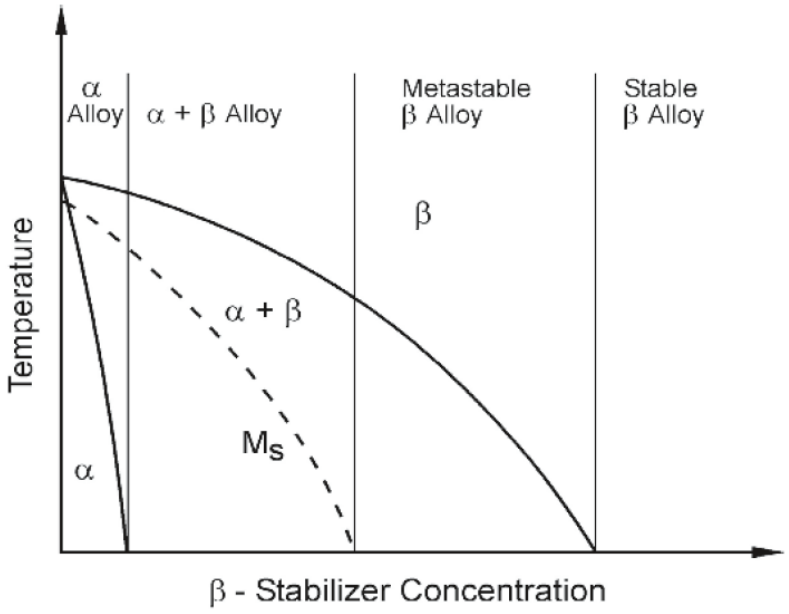

Figure 3.2: Alloy classification according to the content of β stabilizers [9]

3.1.1 Ti and Ti-alloys for biomedical applications

Biomedical applications need a material that fulfills the following requirements:

- Biocompatibility (i.e. it must not cause any harm to the human body)
- Osseointegration (bioadhesion)
- Appropriate mechanical properties (e.g. similar Young's modulus as bone, sufficient fatigue strength)
- High corrosion and wear resistance
- Processability and availability

Following these requirements, five groups of metallic materials are standardly used as biomaterials for permanent implants: stainless steel (e.g. X2CrNiMo1812), CoCr-based alloys (e.g. CoCr30Mo6), titanium and its alloys, CP-niobium and CP-tantalum. Among these, Ti and Ti-alloys show the best combination of required properties [3].
The first generation of biomedical titanium alloys is dominated by commercially pure titanium (CP-Ti) and Ti-6Al-4V and they are still most commonly used for implant applications [1]. However, there is a concern about the biocompatibility of vanadium and aluminum [12]. To overcome this issue, β-Ti alloys were developed excluding cytotoxic elements or elements that cause allergic effects or neurological disorders. Several studies reveal that β-stabilizing elements such as Nb, Ta, Zr, Sn and Mo show enhanced biocompatibility [13, 14]. Moreover, β-titanium alloys show the lowest Young's modulus (50-80 GPa) among all permanent metallic biomaterials. This fact is beneficial with regard to the stress-shielding effect, i.e. the possible resorption of bone followed by implant loosening, which occurs because of different Young's moduli between bone (10-40 GPa) and implant material [1]. Some exemplary β-titanium alloys are: Ti-12Mo-6Zr-2Fe (TMZF^{TM}), Ti-13Nb-13Zr, Ti-15Mo, TIMETAL® 21SRx and Tiadyne 1610 [15].

3.2 Metal Injection Molding

Metal injection molding (MIM) is a near-net-shape powder metallurgy technique that combines the advantages of plastic injection molding with those of powder metallurgy. First demonstrations date back to the 1930s, however, not much attention had been given to this process until the 1970s. Henceforward, continuous process optimization was done and MIM became a leading technology in powder processing [16].

The successful establishment of the MIM process can be explained by the advantages that it offers compared to other fabrication techniques. According to German [16] MIM features the following advantages:

- material flexibility due to the high variety of metal powders available
- prevention/minimization of post processes that enables a high material utilization (near-net-shape technology)
- cost efficient production of complex parts
- high volumes/high production rates

Figure 3.3 depicts the principle of the MIM process. It consists of four key steps: feedstock preparation, injection molding, debinding and sintering. If not quoted elsewise, the following description of the MIM procedure refers to [17], [18] and [19].

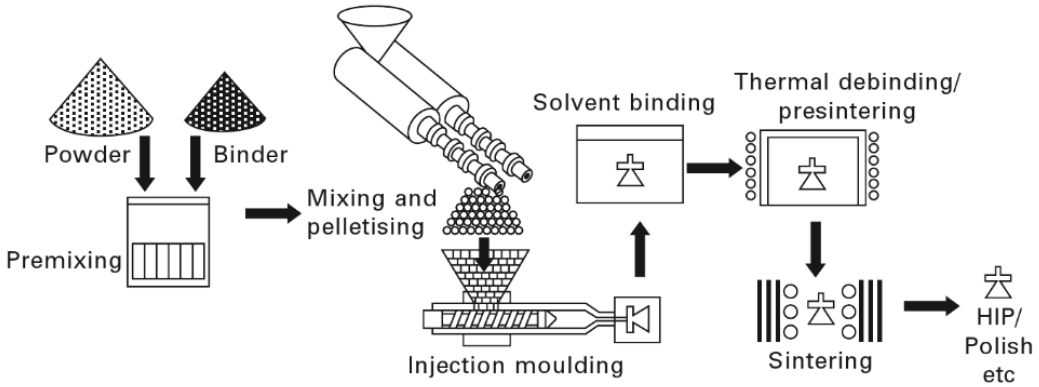

Figure 3.3: Overview of the MIM process [18]

3.2.1 Preparation of the feedstock

The starting material for the MIM process is called feedstock. It is a mixture of metal powder and binder in a certain ratio. The characteristics of the feedstock, such as rheological properties (flowability), viscosity, homogeneity and powder load, essentially affect the quality of the molded part and final product. Powder, binder, powder/binder ratio and mixing technique are influencing the feedstock and, therefore, a proper combination of all these factors is necessary to obtain satisfactory results.

Powder

The ideal MIM powder should have the following characteristics:

- tailored particle size distribution with small mean particle size (<45 µm)
- dense particles but no agglomeration
- spherical particles
- high purity level and clean surface
- minimum explosivity and toxicity

The use of small particles allows rapid sintering with small molding defects. Due to the fact that there is more contact between particles, friction is higher and distortion can be avoided. The appropriate particle size distribution and particles without voids enable a high packing density and less shrinkage. High packing density is also achieved by spherical particles, although slightly irregular shaped particles have the advantage of a better shape retention. Especially powders with a small particle size are very affine to oxygen pickup. Therefore, powders are preferentially handled under protective atmosphere to keep contamination to a minimum.

Powders used in MIM are primarily fabricated by gas or water atomization, thermal composition or chemical reduction. In case of Ti-MIM, plasma atomized and hydride-dehydride (HDH) powders are widely used [20]. Atomized powders have spherical shape and high purity, but they are also more expensive. A combination with low cost powders like HDH powders is possible, but their irregular shape and lower purity levels have to be considered.

To obtain the desired alloying composition, there are three different possibilities: blending elemental powders in the correct ratios (elemental method), using powder with the right stoichiometry (pre-alloyed method) or mixing elemental powder with powder that is enriched in certain alloying elements (master alloy method). The use of pre-alloyed powder is advantageous with regard to homogenization, but compressibility and sintering can be influenced negatively due to solid solution hardening caused by the alloying elements (e.g. in Fe-Sn and Fe-Mo sintering alloys) [21].

Binder

The properties of the binder play a crucial role in the whole MIM process. The principal task of the binder is to enable shaping during injection molding and to hold this shape until sintering. There are different requirements that the binder has to fulfill concerning powder interaction, flow characteristics, debinding and manufacturing. For example, the binder should be able to fully surround the powder particles (low contact angle). However, binder

and powder should be inert with respect to each other. Furthermore, the binder should be cheap and should not deteriorate until debinding. Fast removal without the formation of corrosive or toxic products is also desirable.

To succeed these requirements, a multi-component system is usually used. One of the main components is a polymer backbone, for example ethylene vinyl acetate (EVA) or polyethylene (PE), which provides strength. Another important component is a filler polymer such as wax that decomposes at lower temperatures and enhances the flowability of the feedstock. Eventually, lubricants (e.g. stearic acid) can be added to improve the bonding between powder and binder.

Mixing

Mixing is carried out under the influence of temperature and shear between the particles to ensure a homogenous feedstock. The procedure can be either carried out in a batch process (e.g. Z-blade mixers) or continuously (e.g. screw extruders).

After mixing, the feedstock is cooled down and granulated to gain a pelletized mixture ready for injection.

3.2.2 Injection molding

A schematic graph of a common injection molding machine can be seen in Figure 3.4. First, the feedstock is poured in the hopper and transported into the heated barrel by a reciprocated screw. In the barrel, the feedstock is homogenized and starts to melt. By a thrust of the screw, the molten feedstock is then injected through a nozzle into the mold. As the mold cools down, the feedstock solidifies again and the so-called green part can be ejected.

Molding parameters such as mold and injection temperature, injection speed, pressure and cooling time have to be adapted to the feedstock.

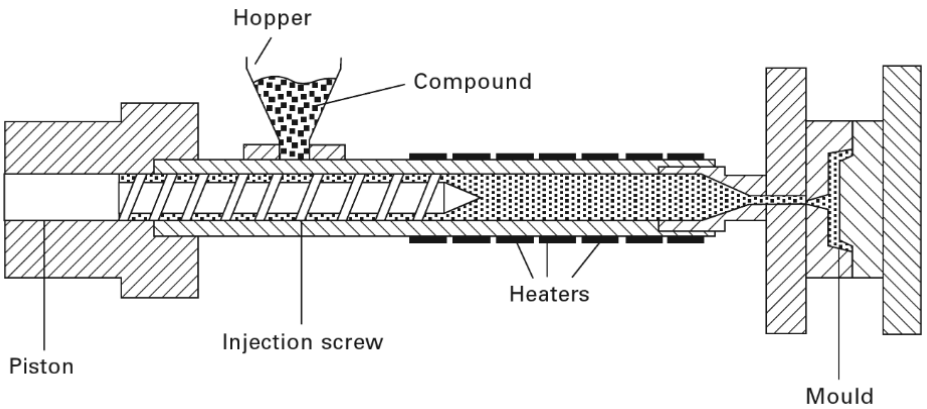

Figure 3.4: Schematic graph of a basic injection molding machine [18]

3.2.3 Debinding

After injection molding, the binder system has to be removed. Debinding is the most critical and costliest step in the whole process. Usually, it is carried out stepwise to ensure an effective binder removal without causing any damage to the parts, such as cracks, distortion or contamination.

A common procedure, which is also used in this work, is the combination of solvent and thermal debinding. For solvent debinding, the green parts are immersed in a solvent (e.g. hexane). The first binder component is extracted and leaves a network of open pores. The second binder (backbone polymer) can then evaporate through these pores during thermal debinding, where sweep gas like argon is used to enhance the binder transport out of the furnace.

3.2.4 Sintering

Sintering is a thermal treatment and the final step of the MIM process. During sintering, pores are eliminated and the loosely bonded powder particles transform into a coherent, solid mass. Sintering is usually performed at 2/3 to 4/5 of the melting or solidus temperature (in Kelvin). For powder mixtures, the sintering temperature refers to the temperature of the lowest melting phase. The driving force of the sintering process is the minimization of the free energy of the system. In case of powders, this means the reduction of all inner and outer surfaces (powder particle boundaries, pores, grain boundaries) as well as homogenization for multiple-phase systems [21].

To achieve this reduction of energy, a high amount of material movement is necessary. The mass transport mechanisms can be seen in Figure 3.5. They are divided in two main classes: surface transport (surface diffusion (1), lattice diffusion from surface (2), vapor transport (3)) and bulk transport (grain boundary diffusion (4), lattice diffusion from grain boundary (5), plastic flow (6)). All of these mechanisms lead to neck growth, but only bulk transport contributes to densification [22].

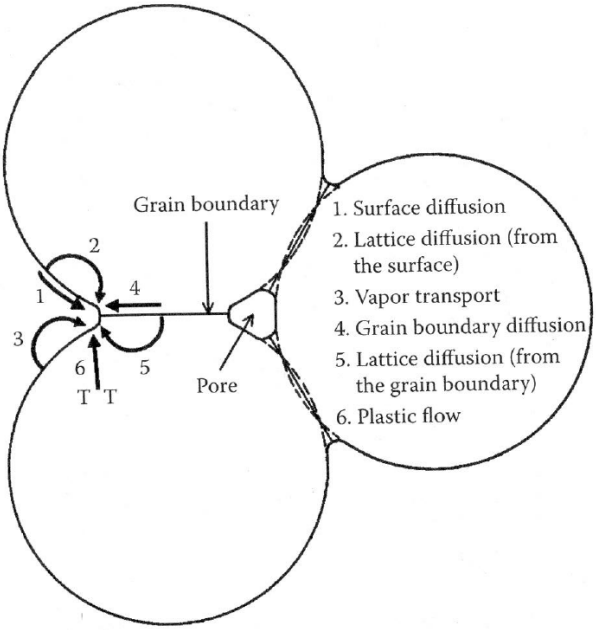

Figure 3.5: Transport mechanisms during sintering [23]

Sintering basically consists of three stages [22]:

- Initial stage: This stage is characterized by neck formation between contacting particles. The neck size is still small and the shrinkage is low. The pores are mainly angular and interconnected.
- Intermediate stage: This stage is dominated by large densification and shrinkage. The pores are rounded and still interconnected. They generally remain on grain boundaries and prevent grain growth, but at the end of this stage, coarsening can occur.
- Final stage: The connected pore structure collapses into isolated, spherical pores. This process starts at about 15% porosity and by 5% porosity, all pores are closed. In atmosphere-based sintering, full density is not possible due to trapped gas in the pores. Furthermore, isolated pores that are located inside grains cannot be eliminated completely, because only volume diffusion is possible, which is very slow. During the final stage, shrinkage slows down and grain growth starts.

3.3 Ti and Ti-alloys processed by MIM

As already mentioned titanium and its alloys are applied in several fields due to their specific properties, such as high specific strength, excellent corrosion resistance and high biocompatibility. However, the rather high costs of raw material and machining often limit the applications. To overcome this problem, MIM with its typical advantages appears as a good alternative compared to other processing methods [5].
Current applications of Ti-MIM can be found in three different areas, depending on powder and process quality: decorative items (e.g. watch cases), mechanical components (e.g. surgical tools) and life critical applications (biomedical implants) [20]. Concerning the biomedical sector, CP-Ti, Ti-6Al-4V and Ti-6Al-7Nb are the most common alloys and several applications have already been established successfully on the market. Besides, efforts are made to develop the MIM route also for other titanium based alloys [24].

Although MIM of titanium is a promising procedure, it is still rather unusual and there are some aspects that have to be considered. One of the most challenging factors is definitely the content of interstitial elements, especially oxygen and carbon, which strongly affect the mechanical properties. Interstitials increase strength and hardness, but concerning ductility, they are very detrimental if a certain level is exceeded. Consequently, contamination during the whole process has to be controlled. The most critical factors for the oxygen pick-up are the initial purity of the powder and the furnace atmosphere that has to be as clean as possible. Carbon is introduced by the binder and can react with titanium during debinding. To keep the carbon absorption at a minimum level, optimization of process parameters and binder composition is necessary [5]. Final impurity levels that can be achieved in the MIM process of Ti-6Al-4V are typically 0.20-0.22 m.% oxygen and 0.04 m.% carbon [20].
Another challenge of the MIM process is residual porosity. Typical values of the density are around 96-97%, but with additional hot isostatic pressing (HIP) this can be improved to practically 100%. High densification is important to avoid the deterioration of mechanical properties [5].
In terms of medical applications excellent biocompatibility is essential. It is not fully clarified if the MIM process influences the biocompatibility of titanium alloys. The few publications concerning this topic have been summarized by Sidambe [25]. Investigations include MIM CP-Ti, Ti-6Al-4V and Ti-6Al-4V-0.5B and none of them show any toxicity. Furthermore, initial cell adhesion and cell proliferation of MIM CP-Ti and Ti-22Nb in comparison with arc-melted Ti-22Nb was investigated by Zhao [6]. He showed that MIM samples exhibit better cell

growth, which is probably due to the higher surface roughness. The positive effect of a rougher surface has also been reported by other researchers [26, 27].

German [20] summed up all challenges of Ti-MIM in four critical factors, namely density, purity, alloying and microstructure, which have to be considered for the successful metal injection molding of titanium. He also gives a good overview of the basic steps and common practices of the Ti-MIM process.

3.3.1 Ti-Nb alloys processed by MIM

Ti-Nb alloys are, like β-titanium alloys in general, a promising alternative for medical implants due to their better biocompatibility and lower Young's modulus. The idea of combining the good properties of Ti-Nb alloys with the advantages of MIM seems interesting and first attempts have already been reported. Ti-17Nb alloys (m.%) were successfully produced via the MIM route by Bidaux *et al.* [28, 29]. Sintering behavior, microstructure, mechanical properties and cytocompatibility of MIM Ti-Nb alloys were also studied by Zhao [6]. Ti-Nb alloys were fabricated by MIM using elemental powders with 10, 16 and 22 m.% niobium content. CP-Ti served as a reference. The increasing Nb-content led to higher porosity, which can be attributed to the influence of niobium on the sintering process. The diffusion of Nb atoms and the associated homogenization between titanium and niobium starts at higher temperatures (>900 °C). At lower temperatures, niobium particles act as diffusion barrier.
Zhao also discovered that in the case of MIM processing niobium leads to the formation of titanium carbides, which precipitate preferentially at grain boundaries. This is also observed for Ti-15Mo [30], but not for other titanium alloys like CP-Ti or Ti-6Al-4V. Thus, the assumption was made that the addition of niobium or molybdenum decreases the carbon solubility and favors carbide formation. In both cases, the carbides were identified as fcc Ti_2C by TEM investigations [30, 31].

Zhao's work revealed that carbide precipitates have, besides the solid solution strengthening effect caused by niobium atoms, a positive effect on tensile strength, but they are detrimental concerning ductility and fracture resistance. Crack initiation and propagation occurs preferentially around carbide particles. Therefore, it is of great interest to control the carbide precipitates with respect to quantity, morphology and distribution.
One possibility to reduce the carbide precipitates is the minimization of the carbon content. Figure 3.6 shows the Ti-22Nb – C phase diagram calculated by ThermoCalc and affirmed by in-situ high energy XRD analysis [6]. The blue shaded area indicates the carbon content that

was observed by Zhao (0.04-0.07 m.%). To completely avoid carbide formation, a limit of 0.023 m.% carbon is predicted. Unfortunately, this is currently not achievable by MIM.

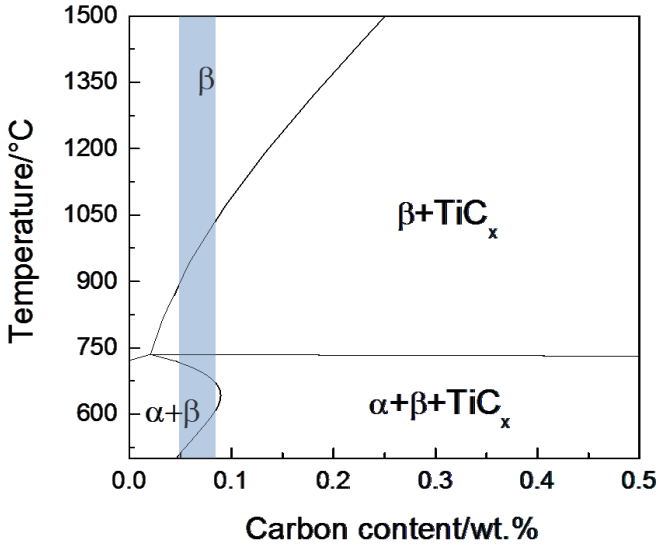

Figure 3.6: Calculated phase diagram of Ti-22Nb – C with the carbon contents of MIM samples produced by Zhao (shaded area) [31]

Another approach that has already been successfully proved is the addition of alloying elements. Beißig [8] investigated the influence of tantalum, boron and zirconium on Ti-Nb alloys. Tantalum showed good results in carbide reduction, but it occurred as challenging concerning the sintering parameters. The addition of boron (0.5 m.%) to Ti-16Nb and Ti-22Nb led to the formation of titanium borides inside the grains and to a carbide reduction. Furthermore, grain refinement and decrease of porosity were observed. Thus, the ductility was enhanced by 2%. In contrast, the addition of zirconium (8.5 m.% to Ti-9.5Nb and 8 m.% to Ti-22Nb) did not improve the ductility, but it showed the strongest influence in carbide reduction.

The positive effect of zirconium was also investigated by Nagaram [7]. He studied the microstructure and mechanical properties of Ti-22Nb with a zirconium content varying between 0-10 m.%. The carbide area fraction and the grain size were reduced, while the porosity increased with zirconium addition. Young's modulus stayed constant (~72 GPa), but strength increased (ultimate tensile strength: 770 MPa to 850 MPa, yield strength: 670 MPa to 740 MPa) and ductility was enhanced from around 2.7% to 5%.

The third possibility to influence the titanium carbides was demonstrated by Zhao [6]. It was shown that the carbide precipitates can be controlled by suitable heat treatments. An annealing treatment at 641 °C for 120 h with subsequent water quenching to room

temperature was performed in order to dissolve the titanium carbides. The amount of carbides could be decreased and, moreover, the as-quenched samples revealed adequate mechanical properties for an application as implant material.

However, the mechanisms behind are not fully understood and, therefore, further investigations concerning the influence of heat treatments on carbide reduction in Ti-Nb alloys are necessary.

4 Experimental procedures

4.1 Sample preparation

Four different compositions were studied in this work: Ti-22Nb, Ti-22Nb-10Zr, Ti-22Nb-10Zr-0.3B and Ti-22Nb-10Zr-0.5B (all m.%). According to their elemental composition, abbreviations will be used as follows:

- **TN** for Ti-22Nb
- **TNZ** for Ti-22Nb-10Zr
- **TNZ3B** for Ti-22Nb-10Zr-0.3B
- **TNZ5B** for Ti-22Nb-10Zr-0.5B
- **TNZxB** for both Ti-22Nb-10Zr-0.3B and Ti-22Nb-10Zr-0.5B

Samples were prepared by two powder processing routes: a) manual pressing of feedstock and sintering and b) MIM. The starting materials are elemental powders as listed in Table 4.1.

Table 4.1: Summary of used powders

Powder	Particle size	Producer
Titanium (grade 1), spherical	<45 µm	AP&C, Canada
Niobium, angular	<110 µm	MHC Industrial, China
Zirconium, spherical	<45 µm	TLS Technik, Germany
Boron (amorphous), angular	<1 µm	H.C. Starck, Germany

For feedstock preparation the metal powders were added with 8 m.% of binder consisting of 60 m.% paraffin wax, 35 m.% ethylene vinyl acetate and 5 m.% stearic acid. Powders and binder were weighed under argon atmosphere in a glove box, heated up to about 115 °C and then mixed in a Thinky ARE-250 planetary mixer until homogeneity was reached. Then the finished feedstock was granulated manually.

Cylindrical parts of each composition TN, TNZ and TNZxB were produced by manual pressing under air. A die of 8 mm inner diameter was heated up to 120 °C and feedstock was added. Then the molten feedstock was uniaxially pressed with a force of 2.5 kN using Enerpac hydraulic press and cooled down by a fan.

Manually pressed samples are too small for XRD analysis. Therefore, discs from TN and TNZ were injection molded on a MCP 100KSA (HEK GmbH) plunger injection molding machine. The injection parameters are shown in Table 4.2.

Table 4.2: Parameters of injection molding

Injection temperature	Mold temperature	Injection time	Injection pressure
120 °C	45 °C	1 s	6 bar

In all cases the green parts were solvent debinded in hexane at 40 °C for 900 min in a LÖMI EBA 50 debinding device.

Thermal debinding and sintering were carried out in one cycle on a XERION XVAC 1600 furnace. Thermal debinding was done in two steps of 1 h at 450 °C and 1 h at 600 °C under argon flow. Sintering was done at 1500 °C for 4 h under vacuum atmosphere.

Two sintering cycles, namely standard sintering and fast cooled sintering, were carried out. Standard sintering was performed at a cooling rate of 10 K/min under vacuum. For fast cooled sintering, the temperature decrease was set directly from 1500 °C to 0 °C after sintering and argon flow was switched on. By this, an average cooling rate of 75 K/min down to 900 °C was achieved. At lower temperatures the cooling rate decreased, because heat emission was insufficient.

The temperature sequences of the two sintering cycles are shown in Figure 4.1. The solid lines mark the set values, while the dashed lines present the real values.

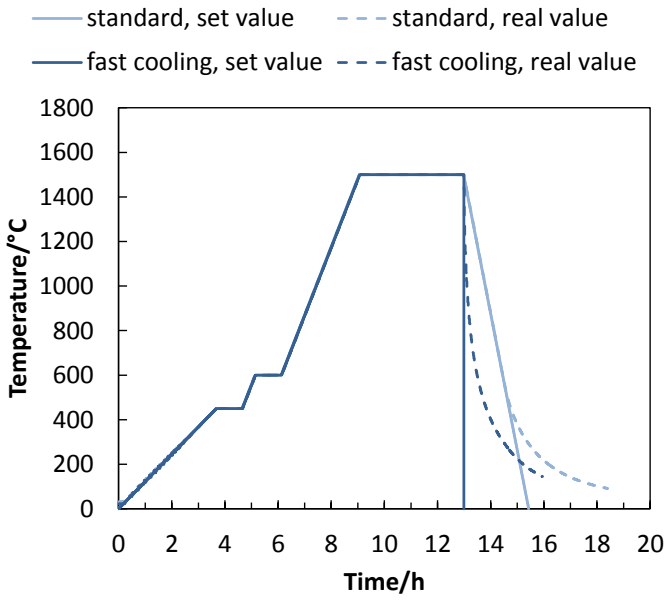

Figure 4.1: Temperature sequences of the two sintering cycles

A picture of the sintering plates and rings used as support is shown in Figure 4.2. The number of sintered samples is noted next to that. The standard sintering was done on two plates, while the fast cooled sintering was done with fewer parts on one plate.

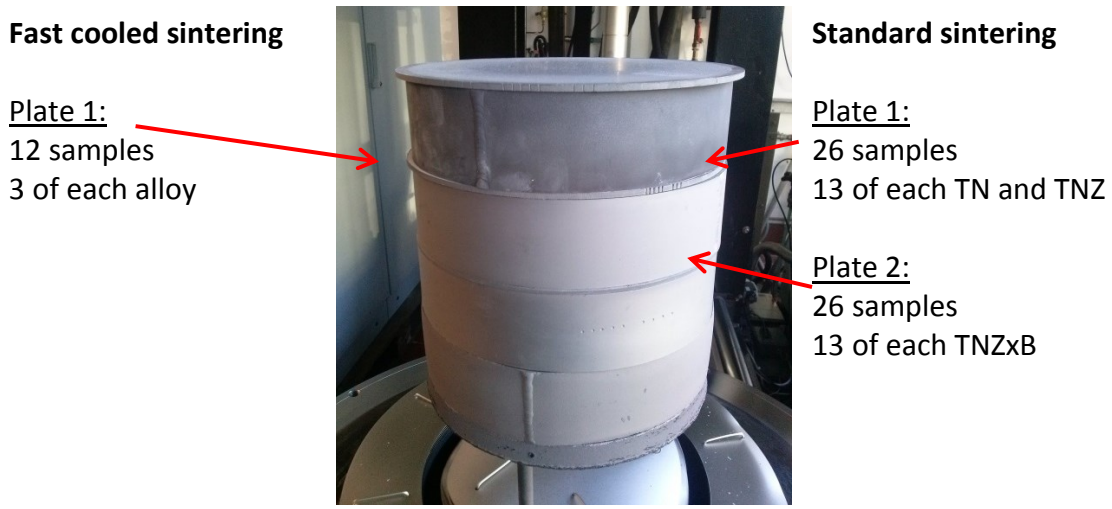

Figure 4.2: Sintering plates and rings with a description of the sample arrangement during the two sintering cycles

To control the binder removal during processing, every sample was weighed (FZ-300i balance, A&D Company) and their size was measured with a caliper. Figure 4.3 displays a comparison between green parts and as-sintered parts produced by manual pressing (left), and a disc prepared by MIM (right).

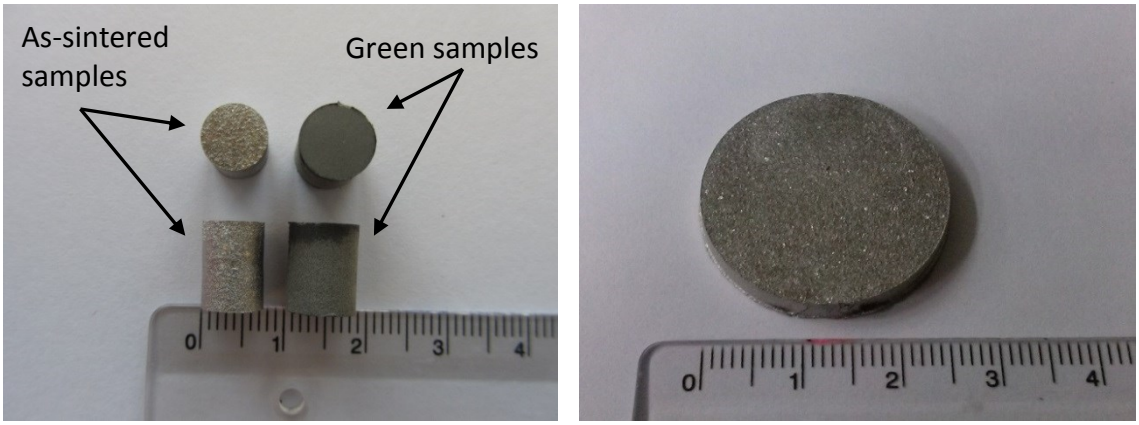

Figure 4.3: Manual pressed green and sintered parts (left), sintered MIM specimen (right)

4.2 Heat treatments

Heat treatments were performed on manually pressed and injection molded samples consolidated by the standard sintering cycle to reduce the quantity of carbides. Three different heat treatments were chosen according to the calculated Ti-22Nb – C phase diagram shown in Figure 3.6:

- **1300** 2 h at 1300 °C and fast cooling to room temperature
- **1300/650** 2 h at 1300 °C, fast cooling to 650 °C, 10 h at 650 °C and fast cooling to room temperature
- **WQ** 10 min at 1300 °C and water quenching to room temperature

All heat treatments included a heating-up to 1300 °C at the beginning in order to fully dissolve the carbide precipitates. The 1300/650 heat treatment additionally contained a holding step at 650 °C, where the carbides are also soluble. Subsequently, the samples were fast cooled (1300, 1300/650) or water quenched (WQ) to suppress the re-precipitation of carbides.

Figure 4.4 shows the set and real temperatures of the 1300 and 1300/650 thermal cycles.

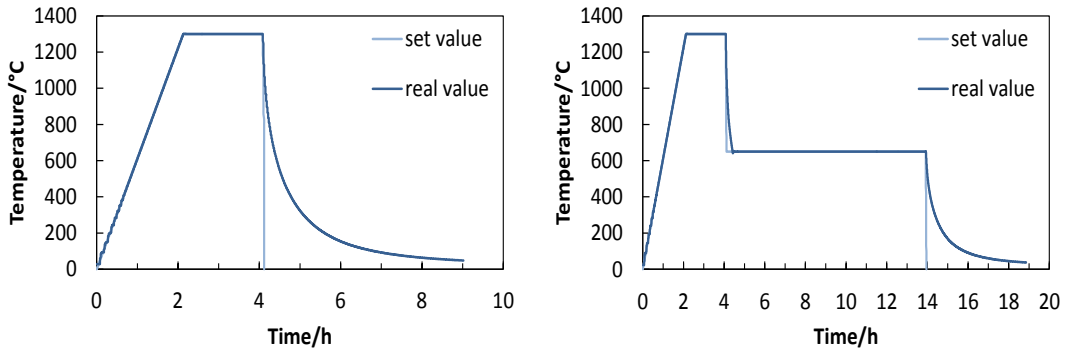

Figure 4.4: Thermal cycles of 1300 (left) and 1300/650 (right) heat treatment with set and real temperature values

Holding steps for 1300 and 1300/650 were conducted under vacuum conditions, while cooling sections were under argon flow. The water quenching was carried out completely under air condition. This causes the formation of an oxide layer on the sample surface. Furnaces used for heat treatments are a XERION XVAC 1600 furnace for 1300 and 1300/650 and a Nabertherm HT 16/16 muffle furnace for WQ.
The list of manual pressed and injected samples and processing parameters can be found in Appendix I.

4.3 Characterization

4.3.1 Chemical analysis

The impurities in the samples were quantified using a LECO melt extraction system. For measuring the carbon and sulfur contents CS-444 device was used. By TC-436, the content of oxygen and nitrogen was determined. Samples from both sintering cycles and from 1300 and 1300/650 thermal cycles were analyzed.

4.3.2 Microscopy

Optical microscope (Olympus PMG3) and scanning electron microscope (SEM) (Zeiss Leo 1530 Gemini) were used for microstructural examination. Specimens were cold embedded and prepared by wet grinding with SiC papers in grit sizes from 320 to 2500 followed by polishing with 3 µm diamond paste and neutral OPS solution.
BSE-images were used for the determination of α and β phase fractions (area%) with the GIMP 2.8 software. One image of each composition was used for the calculation. Compositional analysis was done with energy-dispersive spectroscopy (EDS) using EDAX system. EDS spectra were collected at an accelerating voltage of 15 kV and a measuring time of 100 s.

4.3.3 Determination of carbide and precipitate quantity

Optical micrographs were used for the calculation of carbides and precipitates. Their phase fractions (area%) were determined with the analySIS pro software (Olympus Soft Imaging Solutions). Therefore, it was necessary to set the threshold, which provides the distinction between precipitates and background, very carefully to obtain accurate results. Furthermore, previous image editing was necessary. For TN and TNZ, pores were retouched. The carbides were marked automatically by the software and the carbide area fraction was determined. The precipitate islands in TNZxB could not be marked automatically, because their grayscale was too similar to the background. Hence, all precipitates were first marked manually and the precipitate quantity was then calculated by the software. For the carbide quantity in TNZxB, both pores and precipitate islands were retouched before the determination.
Carbide quantity of all compositions was determined with an average of two images. For TNZxB, only one image was used for the evaluation of the complete precipitate quantity.

4.3.4 Porosity

Porosity of the as-sintered samples prepared by manual pressing was measured graphically with the analySIS pro software and by Archimedes' principle with a respective setup on a Sartorius Master^{pro} scale. The samples are weighed in air and in ethanol and the Archimedes' density is automatically calculated by the equipment. Then, porosity can be determined using

$$P = \left(1 - \frac{\rho_{arch}}{\rho_{th}}\right) \cdot 100 \quad \cdots\cdots (4.1)$$

where ρ_{arch} is the Archimedes' density and ρ_{th} is the theoretical density of the composition. The theoretical density ρ_{th} can be estimated by

$$\frac{1}{\rho_{th}} = \frac{x_1}{\rho_1} + \frac{x_2}{\rho_2} + \cdots + \frac{x_n}{\rho_n} \quad \cdots\cdots (4.2)$$

with ρ_1, ρ_2,…, ρ_n being the theoretical densities of the elements and x_1, x_2,…, x_n being the corresponding mass fractions.

4.3.5 X-ray Diffraction (XRD)

MIM samples of TN and TNZ were characterized by X-ray diffraction on a Siemens D5000 diffractometer. The measurements were carried out on the rotating samples using Cu Kα radiation (0.15418 nm) at 40 kV and 40 A. Specimens were grinded before to obtain a clean surface. Diffractograms were classified using the PDF2002 database of the International Centre for Diffraction Data (ICDD).

4.3.6 Electron Backscatter Diffraction (EBSD)

By Zeiss Ultra 55, electron backscatter diffraction (EBSD) was carried out for all compositions from standard sintering and for 1300 & 1300/650 TN and TNZ. The EBSD images were used for grain size measurement, because the grain boundaries were not possible to determine by optical microscope or SEM, even after etching.

Samples were grinded and polished with a finishing polishing step using a mixture of OPS and H_2SO_4. An area of 2000x3500 μm^2 was measured at 15 kV for 19 h and the grain size was determined with linear intercept technique in the analySIS pro software.

4.3.7 Differential Scanning Calorimetry (DSC)

DSC curves were generated in order to see the phase transformations (i.e. the β transus and probable formation and dissolution of carbides) that are predicted by the pseudo Ti-22Nb – C phase diagram (Figure 3.6). The measurements were performed on a Netzsch DSC 404C and analyzed manually (tangent method) and with Proteus Thermal Analysis software. The specimens were heated up in Al_2O_3 crucibles to 1300 °C and cooled down under continuous argon flow. The heating and cooling rate was 10 K/min. For each alloy one standard sintered sample was used.

5 Results

5.1 The as-sintered samples

5.1.1 Chemical analysis

Impurity levels of oxygen and carbon are shown in Figure 5.1. Fast cooled specimens show generally higher O-content than those from standard sintering. It can be also seen that the oxygen level is increasing with addition of zirconium and boron in fast cooled sintered samples, while it remains steady for standard sintered samples.

From the results of C-content, it can be seen that fast cooled samples are in a range of 0.11-0.13 m.% with slightly higher values in TNZxB. Regarding to standard sintering, TN and TNZ show higher and TNZxB lower C-content than fast cooled sintering.

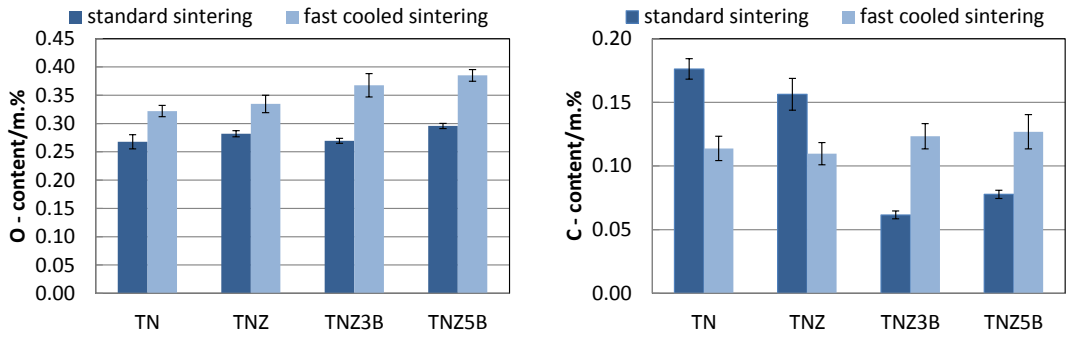

Figure 5.1: Chemical analysis of oxygen content (left) and carbon content (right)

5.1.2 Porosity

Table 5.1 summarizes the porosity of the manually pressed samples after sintering. There is no difference between standard sintering and fast cooled sintering, but the effect of zirconium and boron addition can be seen. The porosity increases with zirconium and boron being added to the base TN alloy.

Different values for Archimedes' porosity and porosity determined by microscopy (image analysis) can be observed. The image analysis always shows higher porosity, where specimens containing boron show the biggest differences.

Table 5.1: Porosity

	Sintering cycle	Archimedes' porosity/%	Image analysis/%
TN	Standard sintering	4.72	4.72
	Fast cooled sintering	4.73	5.18
TNZ	Standard sintering	5.90	7.28
	Fast cooled sintering	5.68	7.30
TNZ3B	Standard sintering	7.87	9.16
	Fast cooled sintering	7.72	9.14
TNZ5B	Standard sintering	8.39	10.33
	Fast cooled sintering	8.21	9.58

5.1.3 Optical microscopy and quantity of precipitates

Figure 5.2 shows the optical micrographs of the fast cooled samples. Images of standard sintered samples are not shown at this point, but they can be found in chapter 5.2.2 (p.33) when they are compared with heat treated samples. Considering the fluctuation of C-content in standard sintered samples visible in Figure 5.1, conclusions about the effect of zirconium and boron on the precipitate quantity are only drawn from the results on fast cooled samples.

All as-sintered specimens basically present the same microstructure (see e.g. Figure 5.2 for fast cooled sintering). In every sample, pores with different size and shape are seen. The increase of porosity of TN samples by adding zirconium and boron is observed, with the pores getting more and bigger.

Homogeneously distributed precipitates can be found in all compositions (marked with arrows in Figure 5.2). These elongated precipitates should be carbides. The addition of boron results in further precipitates assumed to be borides. They are arranged like islands all over the matrix. These islands have dimensions up to 150 µm and consist of angular particles with different sizes (from 5 µm to about 40 µm). Examples of these islands are marked by circles for both TNZ3B in Figure 5.2 (c) and TNZ5B in Figure 5.2 (d).

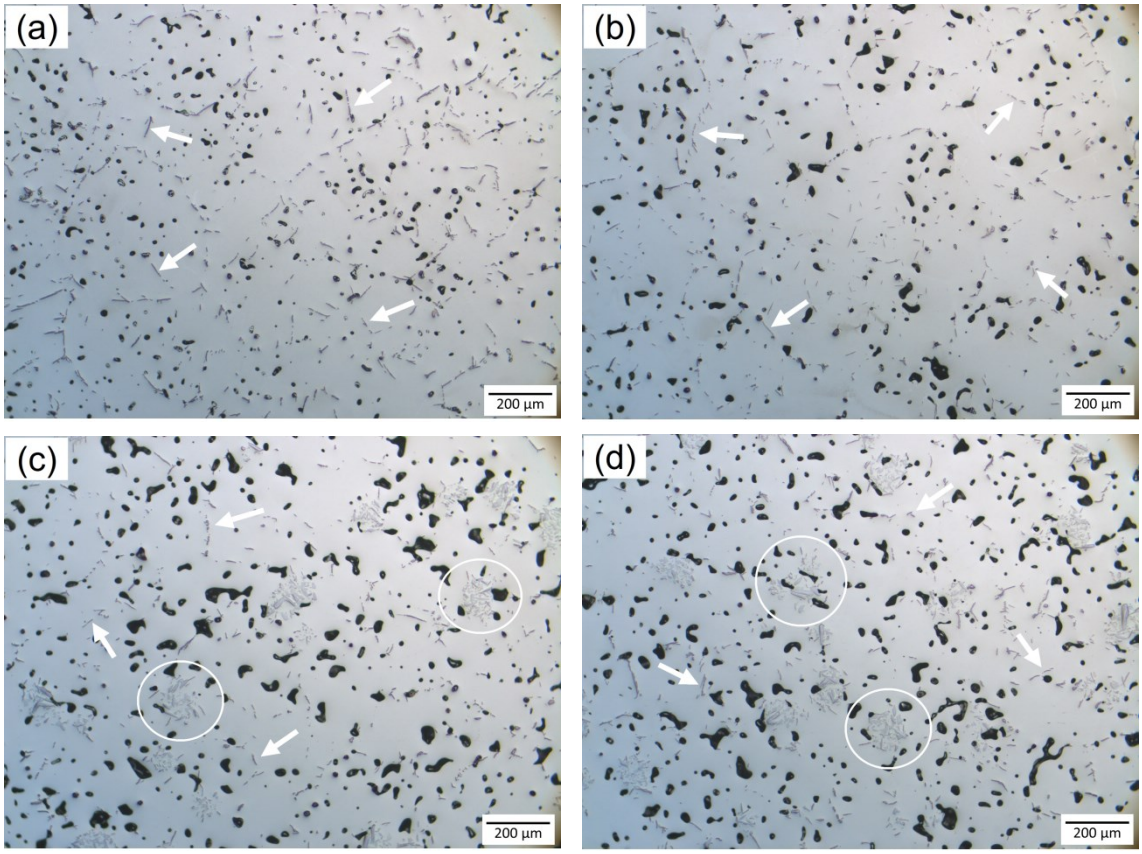

Figure 5.2: Optical micrographs of fast cooled sintered (a) TN, (b) TNZ, (c) TNZ3B and (d) TNZ5B

In TN (Figure 5.2 (a)) mainly long strip shaped precipitates (assumed as carbides) with lengths up to about 85 µm can be found. There is no change in length with addition of zirconium, but reduction in width. In TNZxB the isolated precipitates (assumed as borides) seem to be generally shorter than in TN and TNZ.

The results of the carbide and precipitate (carbides + borides) analysis are summarized in Table 5.2 for standard sintering and in Table 5.3 for fast cooled sintering. The respective C-contents are also depicted. For the carbide quantity in TNZxB, island precipitates are not considered. It can be seen that a higher C-content results in a higher carbide quantity. Furthermore, the results of fast cooled sintering (Table 5.3) reveal that the amount of carbides decreases with addition of zirconium. Further decrease was obtained by the addition of boron, where TNZ3B shows the lowest value of all.

Table 5.2: Summary of carbide and precipitate quantity of standard sintered samples

Alloy	C-content/m.%	Carbide quantity/area%	Precipitate quantity/area%
TN	0.18	3.34	-
TNZ	0.17	2.58	-
TNZ3B	0.06	0.82	2.34
TNZ5B	0.08	0.84	3.91

Table 5.3: Summary of carbide and precipitate quantity of fast cooled samples

Alloy	C-content/m.%	Carbide quantity/area%	Precipitate quantity/area%
TN	0.11	2.79	-
TNZ	0.11	1.82	-
TNZ3B	0.12	1.22	3.62
TNZ5B	0.12	1.50	3.59

5.1.4 SEM and EDS

Some exemplary SE-micrographs showing pores and precipitates are depicted in Figure 5.3. In addition, a basket weave microstructure with dark lamellae (α-Ti) and bright lamellae (β-Ti) is seen in the BSE-images. Figure 5.4 depicts such a α-β microstructure for TN. The thickness of the lamellae varies between 0.2 µm and 0.6 µm and is similar in all alloys investigated.

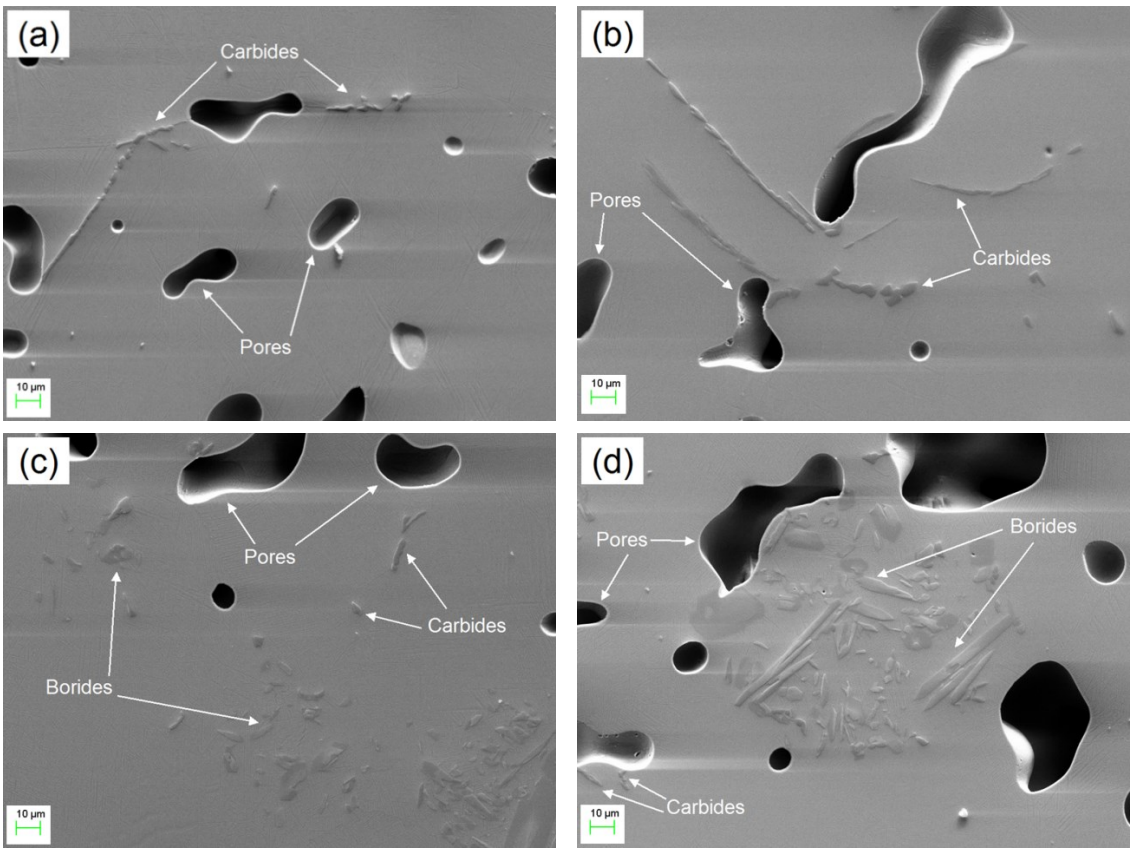

Figure 5.3: SE-images of (a) TN, (b) TNZ, (c) TNZ3B and (d) TNZ5B

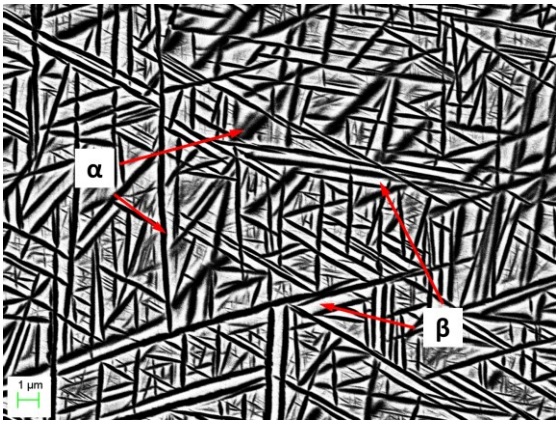

Figure 5.4: BSE-image of TN microstructure with α and β lamellae

EDS measurements were carried out for all alloys in four different regions: α, β, whole α-β structure and precipitates. Figure 5.5 presents exemplary EDS patterns for α-β structure (left) and carbides (right) in TN.

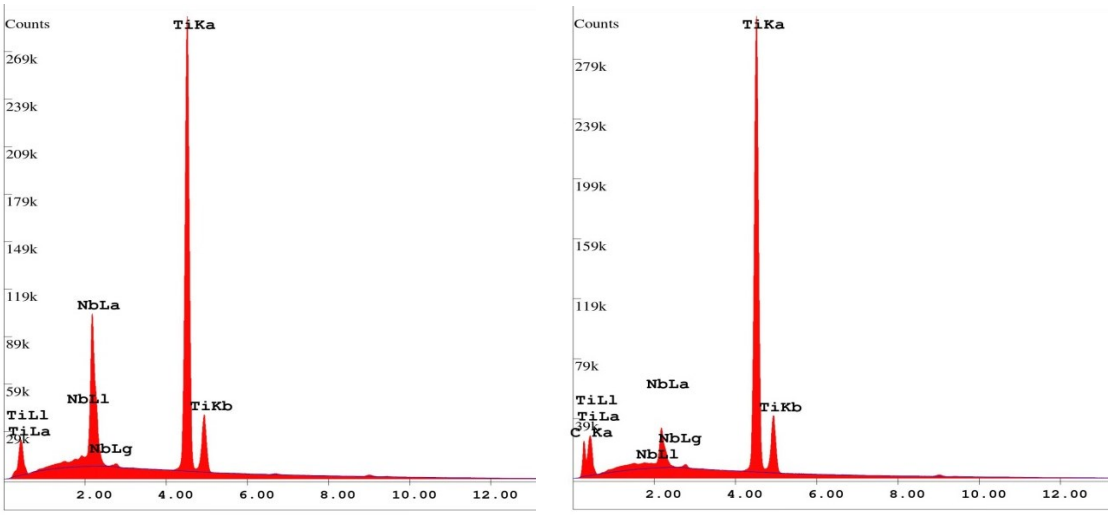

Figure 5.5: EDS patterns of α-β structure (left) and carbides (right) in TN

The EDS results for fast cooled sintering are summarized in Table 5.4. The results for standard sintering will be compared with the heat treated specimens later in chapter 5.2.3 (p. 36) and are not shown here. The values of the α-β structure are in good agreement with the respective alloy compositions. Slight fluctuations are attributed to the accuracy of EDS analysis. Elements are homogeneously distributed in α and β. The elongated precipitates in all specimens are identified as carbides. Their carbon content is similar in all alloys. The zirconium content in the carbides is comparable to that in α and β, while the niobium content is less.

Table 5.4: EDS analysis of the fast cooled samples in at.%

(a) TN

	α-β structure	α	β	Carbide
Ti	86.6	88.1	85.5	66.3
Nb	13.4	11.9	14.5	2.4
C	n/a	n/a	n/a	31.3

(b) TNZ

	α-β structure	α	β	Carbide
Ti	79.2	79.2	79.7	60.5
Nb	13.2	13.4	12.9	3.2
Zr	7.6	7.4	7.5	5.8
C	n/a	n/a	n/a	30.6

(c) TNZ3B

	α-β structure	α	β	Carbide
Ti	79.2	79.2	79.7	60.5
Nb	13.2	13.4	12.9	3.2
Zr	7.6	7.4	7.5	5.8
C	n/a	n/a	n/a	30.6

(d) TNZ5B

	α-β structure	α	β	Carbide
Ti	79.3	78.7	79.1	58.9
Nb	13.0	13.3	13.2	3.0
Zr	7.7	7.9	7.7	5.0
C	n/a	n/a	n/a	33.1

Figure 5.6 shows an example of an island of precipitates with the corresponding EDS results presented in Table 5.5. The precipitates are identified as borides and consist of boron, titanium and niobium. In some cases, also carbides are found among the borides. The EDS analysis as well as the different grayscales in the BSE-image indicates that the borides have a non-homogenous composition. The various grayscales are caused by element contrast. Heavier elements produce more backscattered electrons and result in brighter areas. In this case, the brighter areas of the borides are enriched with niobium. Neither zirconium nor carbon was detected in the borides.

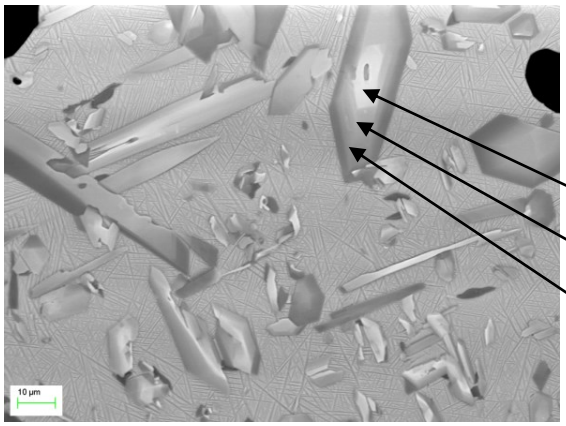

Table 5.5: EDS analysis of one boride (at.%)

	B	Nb	Ti
1	25.4	47.5	27.2
2	23.1	35.9	41.0
3	20.2	19.7	60.1

Figure 5.6: BSE-image of a boride island

5.1.5 Grain size measurement

The result of the grain size measurement of the standard sintered specimens is summarized in Table 5.6. The addition of zirconium and boron leads to smaller grains. This can be also seen from the respective EBSD images in Figure 5.7.

Table 5.6: Grain sizes of standard sintered alloys

	TN	TNZ	TNZ3B	TNZ5B
Grain size/µm	284 ± 148	234 ± 109	168 ± 76	146 ± 65

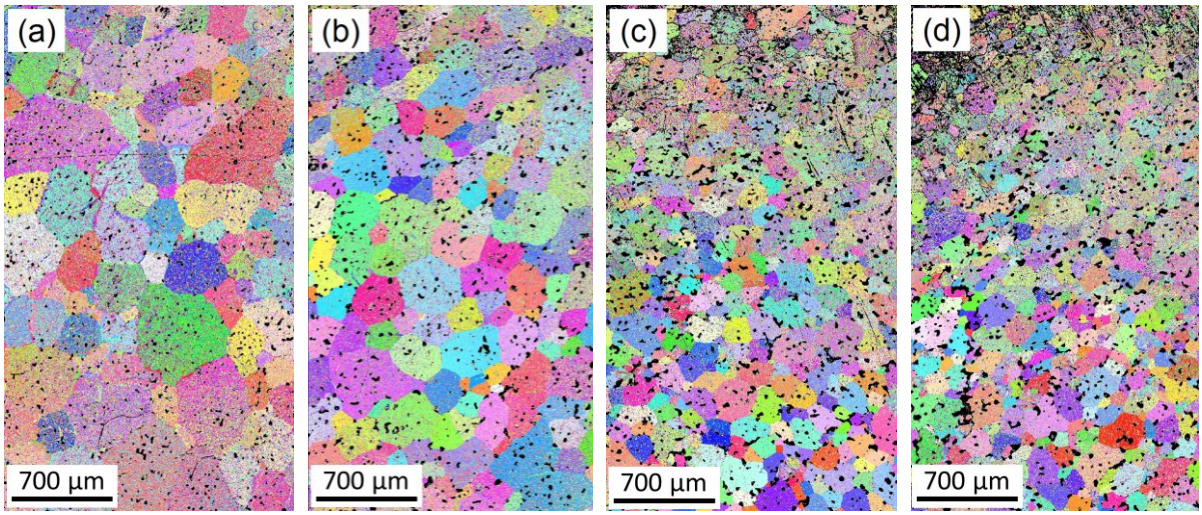

Figure 5.7: EBSD images of (a) TN and (b) TNZ (c) TNZ3B and (d) TNZ5B

5.1.6 XRD

XRD diffractograms of TN and TNZ are shown in Figure 5.8. All peaks could be indexed. The first broad peak belongs to nanocrystalline TiO_2. This TiO_2 is formed on the sample surface as soon as the sample is exposed to air. The other peaks indicate α-Ti and β-Ti and it is observed that they are slightly broadened. Furthermore, a shift of the TNZ diffractogram to smaller angles can be seen. Carbides could not be detected.

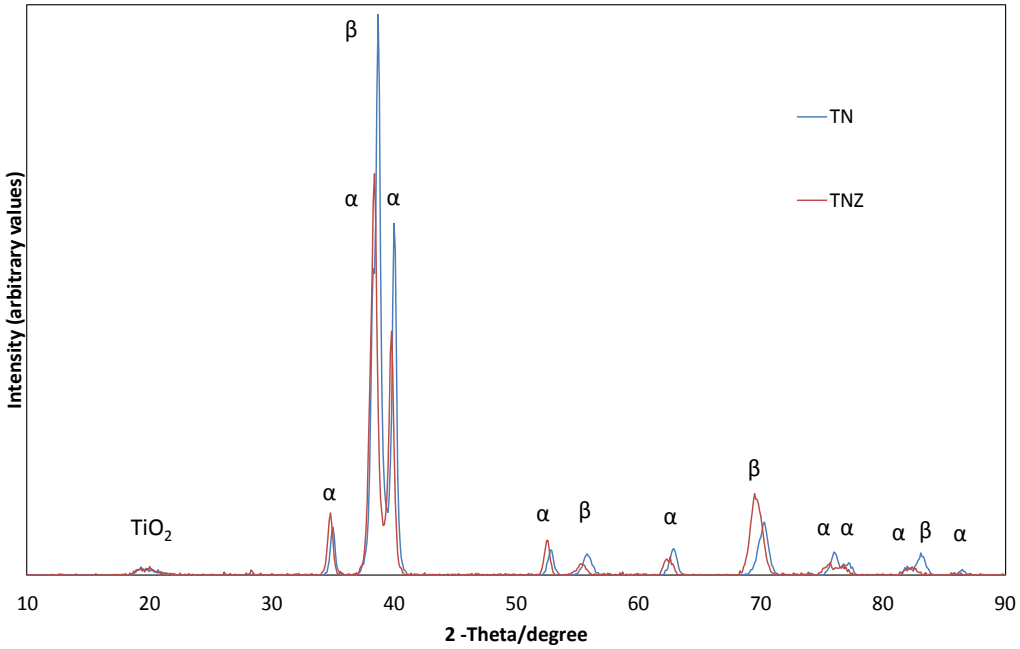

Figure 5.8: Comparison of XRD diffractograms of TN and TNZ

5.1.7 DSC

The DSC heating curves are presented in Figure 5.9. A broad peak can be observed in all alloys (A-D). Peak temperatures were determined manually (tangent method), because the peaks are too flat for software based identification. For TN, the peak temperature was calculated as 695 °C (A). Compared to TN, peaks of TNZ and TNZxB appear at lower temperatures. The peak temperatures are 635 °C for TNZ & TNZ3B (B, C) and 650 °C for TNZ5B (D). Further peaks are observed for TN at 1160 °C (E) and for TNZ3B at 1010 °C (F) and 1170 °C (G).

A single peak can also be seen in the cooling curves shown in Figure 5.10 (H-K), but it is shifted to lower temperatures. The peak temperatures are determined as 595 °C for TN (H), 530 °C for TNZ (I), 533 °C for TNZ3B (J) and 550 °C for TNZ5B (K). Furthermore, the slope of the cooling curves is slightly decreasing above 1000 °C.

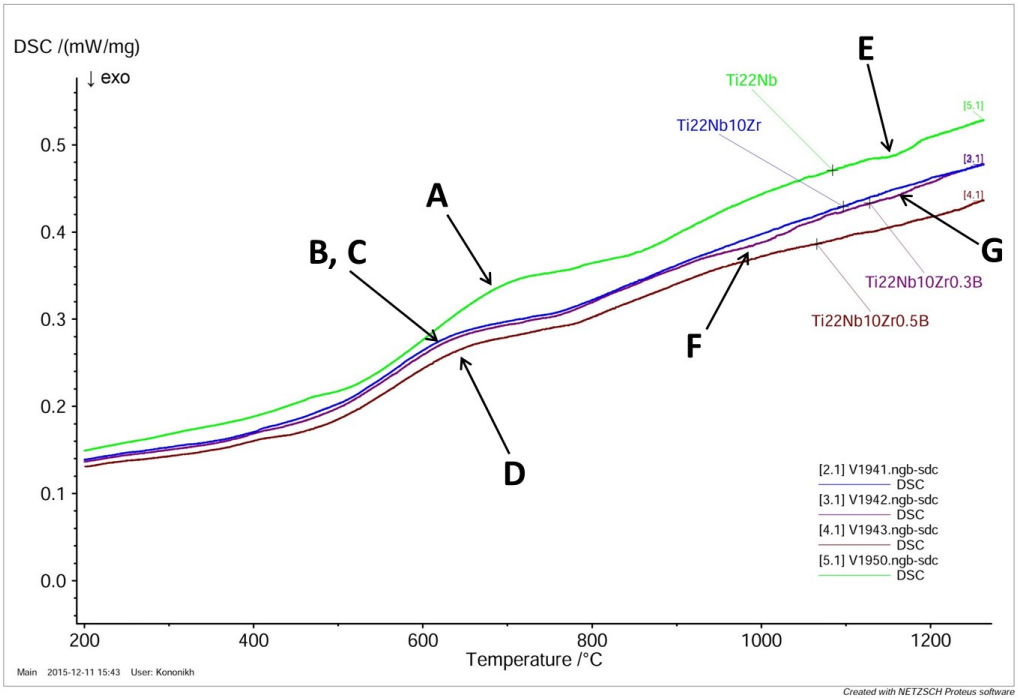

Figure 5.9: DSC heating curves of the as-sintered samples

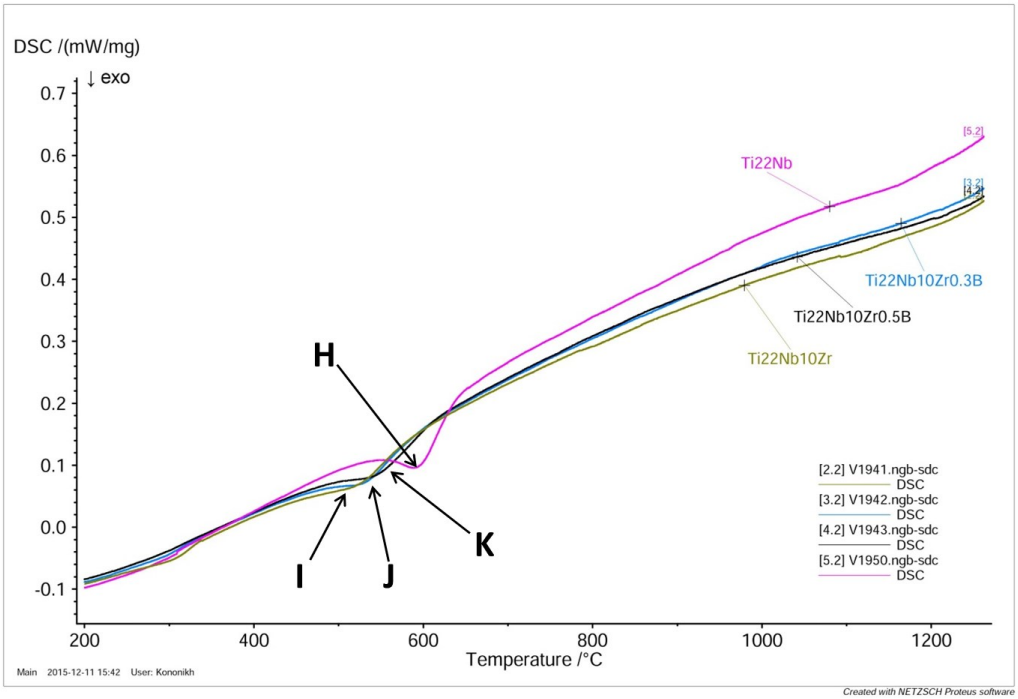

Figure 5.10: DSC cooling curves of the as-sintered samples

5.2 The heat treated samples

5.2.1 Chemical analysis

Table 5.7 to Table 5.10 show the chemical analysis for all compositions before and after heat treating. Slight fluctuations can be seen for the O-content of TN, TNZ and TNZ3B, while it stays steady for TNZ5B. The C-content is slightly varying for TNZ and TNZ3B and stays steady for TN and TNZ5B.

Table 5.7: Chemical analysis of TN as-sintered and heat treated

	O-content/m.%	C-content/m.%
TN	0.27	0.18
TN 1300	0.30	0.18
TN 1300/650	0.29	0.18

Table 5.8: Chemical analysis of TNZ as-sintered and heat treated

	O-content/m.%	C-content/m.%
TNZ	0.28	0.16
TNZ 1300	0.29	0.16
TNZ 1300/650	0.27	0.14

Table 5.9: Chemical analysis of TNZ3B as-sintered and heat treated

	O-content/m.%	C-content/m.%
TNZ3B	0.27	0.06
TNZ3B 1300	0.28	0.08
TNZ3B 1300/650	0.27	0.06

Table 5.10: Chemical analysis of TNZ5B as-sintered and heat treated

	O-content/m.%	C-content/m.%
TNZ5B	0.30	0.08
TNZ5B 1300	0.30	0.08
TNZ5B 1300/650	0.30	0.08

5.2.2 Optical microscopy and precipitate quantity

As already described for the as-sintered samples, pores and precipitates are seen in the optical micrographs. TN specimens before and after heat treatments are shown in Figure 5.11. In the as-sintered condition, the carbides have lengths up to 120 µm and a width up to 10 µm. This stays unchanged after 1300 heat treatment. 1300/650 heat treatment leads to carbides that are shorter and thinner. Carbides are also seen after water quenching, but their size has decreased significantly from about 85 µm to 10 µm. They are located at grain boundaries, but also homogenously distributed in the grains.

The optical images of TNZ and TNZ3B are presented in Figure 5.12 and Figure 5.13, respectively (images of TNZ5B can be found in Appendix II). No obvious effect on the carbides is observed after 1300 and 1300/650 thermal treatments. After water quenching, no carbides are visible anymore. The boride islands stay uninfluenced by all heat treatments.

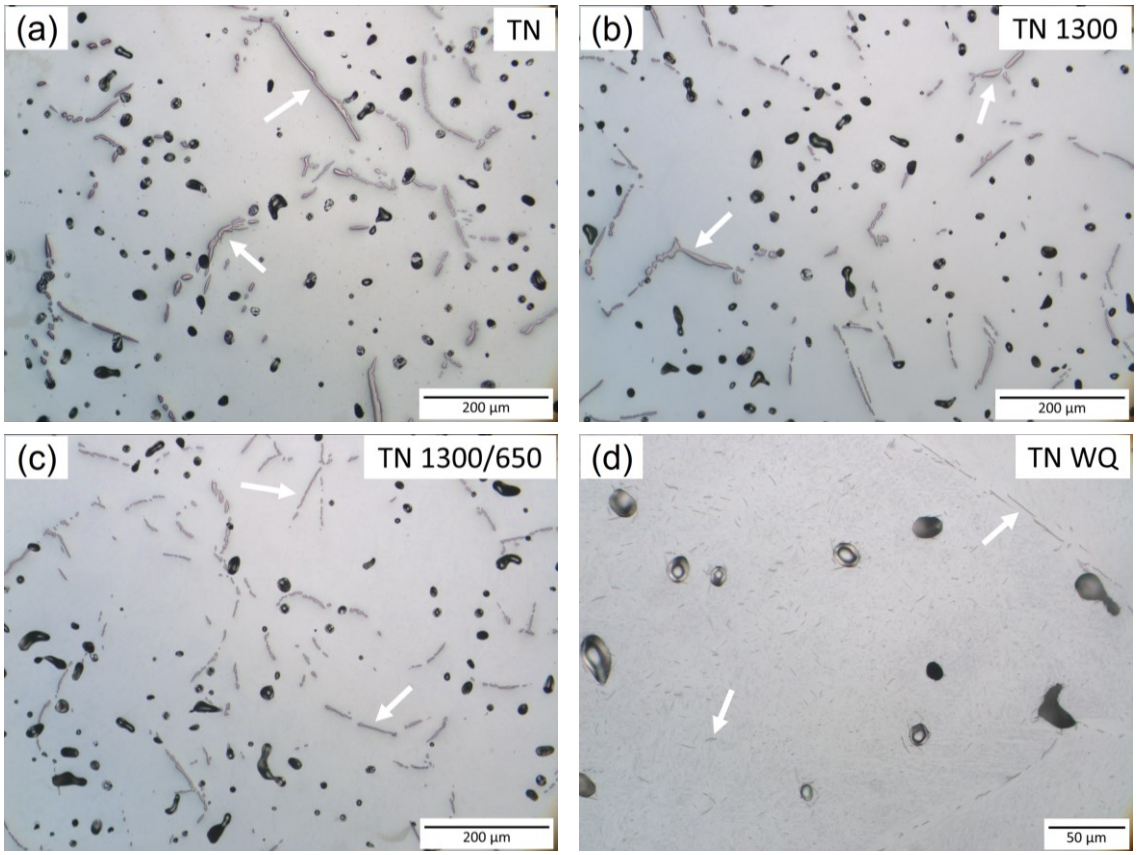

Figure 5.11: Optical micrographs of (a) TN, (b) TN 1300, (c) TN 1300/650 and (d) TN WQ. Carbides are indicated by arrows.

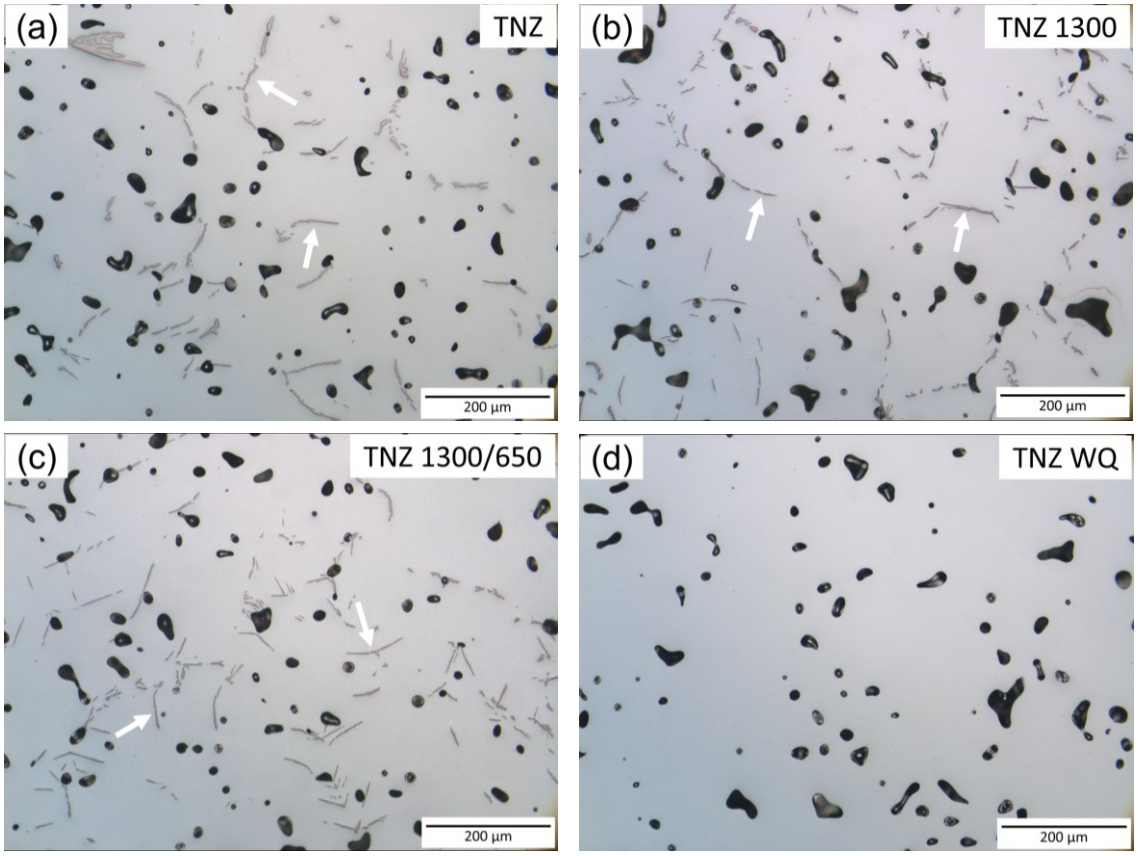

Figure 5.12: Optical micrographs of (a) TNZ, (b) TNZ 1300, (c) TNZ 1300/650 and (d) TNZ WQ. Carbides are indicated by arrows.

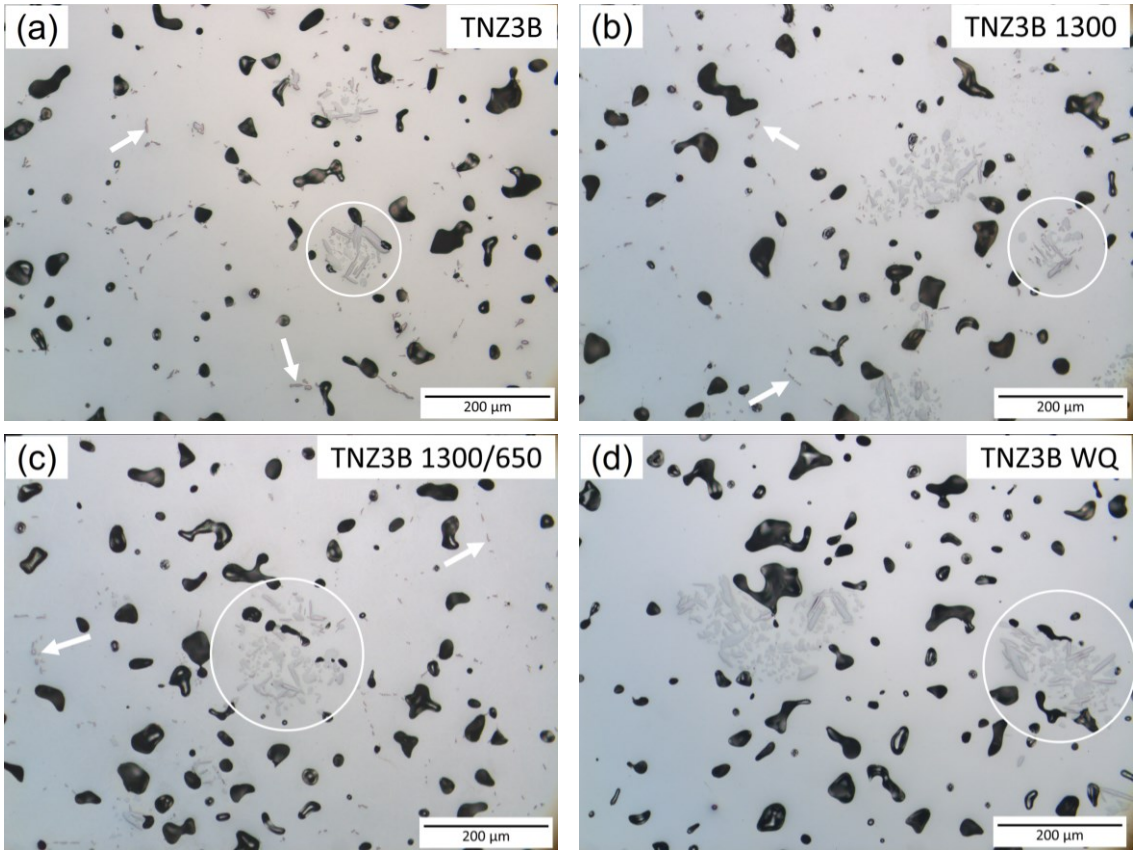

Figure 5.13: Optical micrographs of (a) TNZ3B, (b) TNZ3B 1300, (c) TNZ3B 1300/650 and (d) TNZ3B WQ. Carbides are indicated by arrows. Boride islands are indicated by circles.

Table 5.11 summarizes the precipitate quantity. For TN and TNZ the respective amounts refer to the carbide quantity. For TNZxB the values are presented as "carbide quantity/precipitate quantity", where the precipitate islands are not considered for carbide quantity. The amount of carbides is slightly increasing for 1300 and decreasing for 1300/650 in all alloys. Carbides in TN WQ are visible, but too small for a proper quantitative calculation.

Table 5.11: Summary of carbide and precipitate quantity in area%

	TN	TNZ	TNZ3B	TNZ5B
Standard sintered	3.34	2.58	0.86/2.34	0.84/3.91
1300	3.85	2.64	1.08/2.91	0.87/3.10
1300/650	2.70	2.44	0.80/2.23	0.68/2.42
WQ	-	-	-/2.09	-/2.45

5.2.3 SEM and EDS

Pores, carbides and the α-β basket weave structure can be seen in the BSE-images (Figure 5.14 for TN and Figure 5.15 for TNZ). After 1300 heat treatment there is no change in the α-β structure and the thickness of the lamellae stays in a range of 0.2-0.6 µm. The 1300/650 thermal cycle results in a coarsening of the lamellar structure. The thickness of α lamellae increases to 1-2 µm. It is further noticed that TNZ and TNZxB have larger bright areas (β phase) compared to TN. Very fine lamellae (assumed as secondary α) are observed in these areas. TNZxB show a microstructure similar to TNZ (see Appendix III).

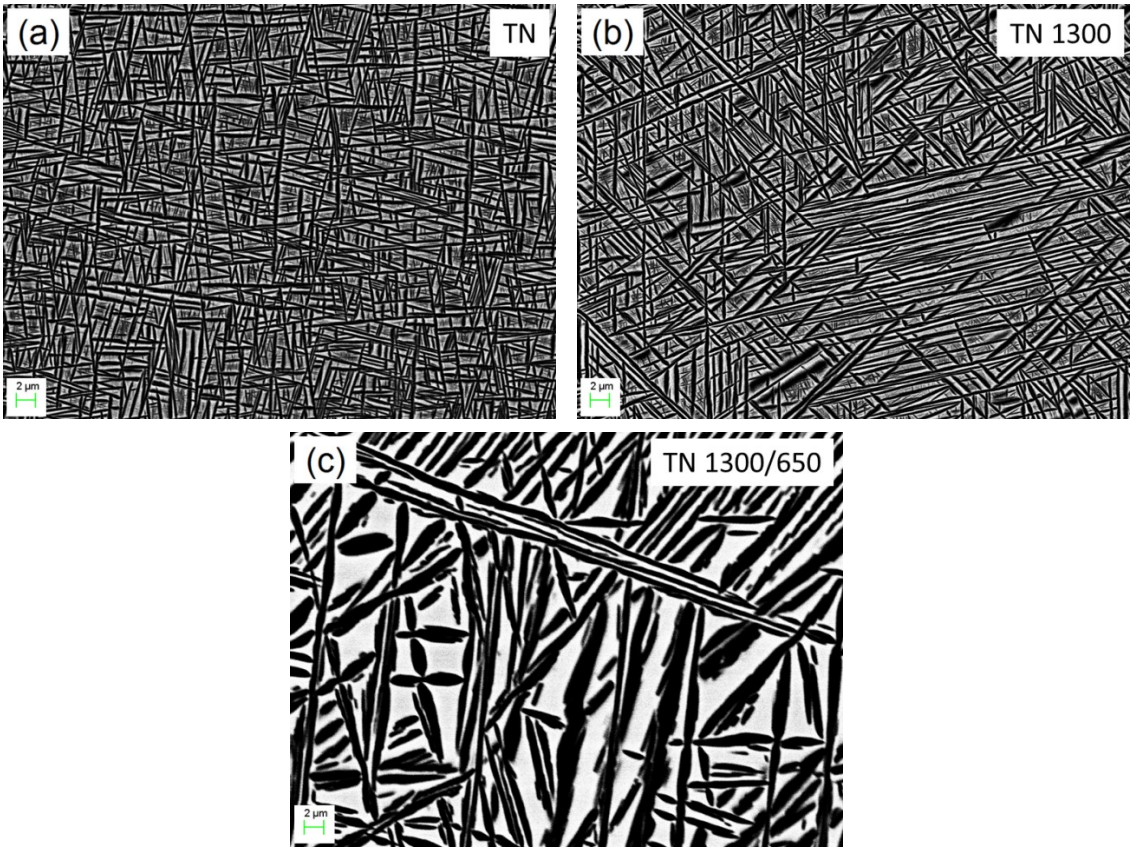

Figure 5.14: BSE-images of (a) TN, (b) TN 1300 and (c) TN 1300/650

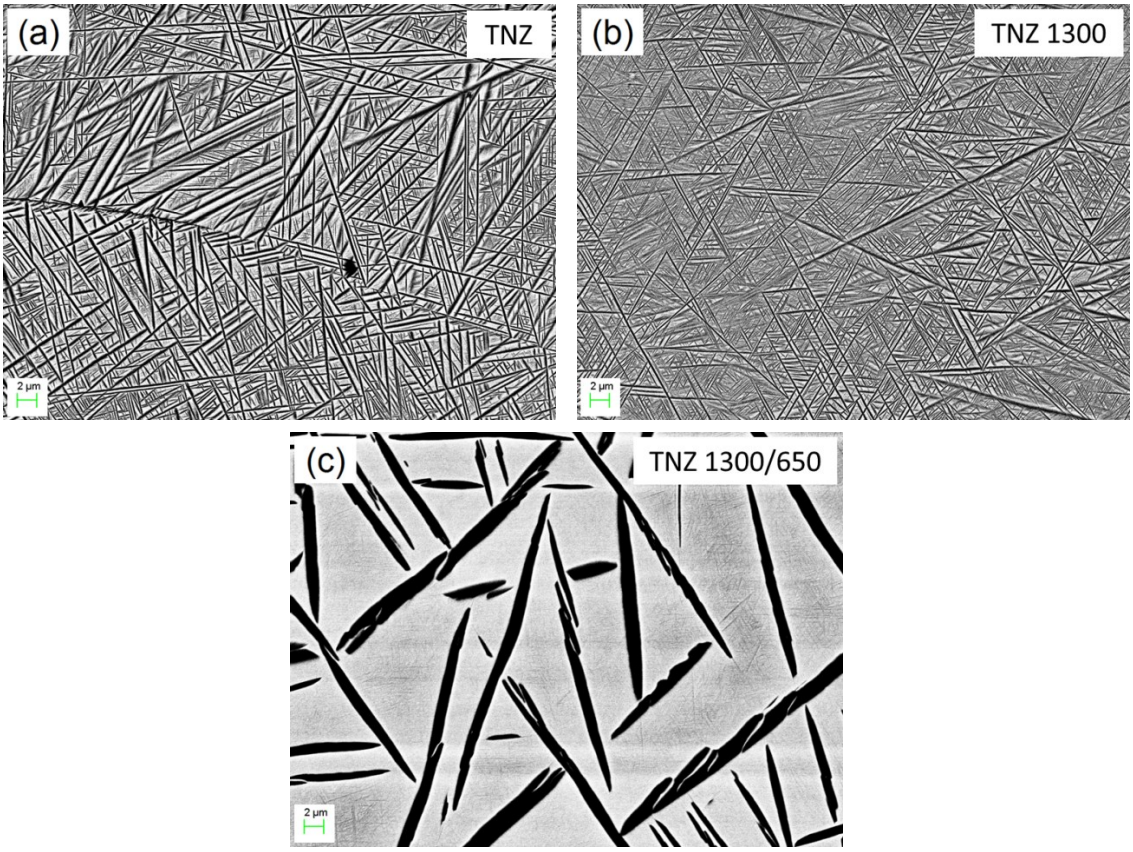

Figure 5.15: BSE-images of (a) TNZ, (b) TNZ 1300 and (c) TNZ 1300/650

Table 5.12 summarizes the phase fractions of α and β in the standard sintered and heat treated samples. It is not possible to make proper conclusions, because only one image was used for the evaluation. However, a decrease of the α phase fraction in TNZ and TNZxB compared to TN is observed. Furthermore, the α phase fraction tends to decrease after the heat treatments.

Table 5.12: Phase fractions of α and β in area%

(a) TN

	α	β
TN	67.5	32.5
TN 1300	65.3	34.7
TN 1300/650	60.1	39.9

(b) TNZ

	α	β
TNZ	52.1	47.9
TNZ 1300	50.1	49.9
TNZ 1300/650	22.7	77.3

(c) TNZ3B

	α	β
TNZ3B	50.4	49.6
TNZ3B 1300	55.5	44.5
TNZ3B 1300/650	33.5	66.5

(d) TNZ5B

	α	β
TNZ5B	57.4	42.6
TNZ5B 1300	53.2	46.8
TNZ5B 1300/650	35.5	64.5

Figure 5.16 depicts TN and TNZ after water quenching (see Appendix III for TNZxB). No basket weave microstructure can be seen in any composition. The small carbides in TN can already be observed with optical microscope. With SEM, very fine precipitates are visible in TNZ, too. They are homogeneously distributed in the grains. In TNZxB, no other precipitates than boride islands are observed.

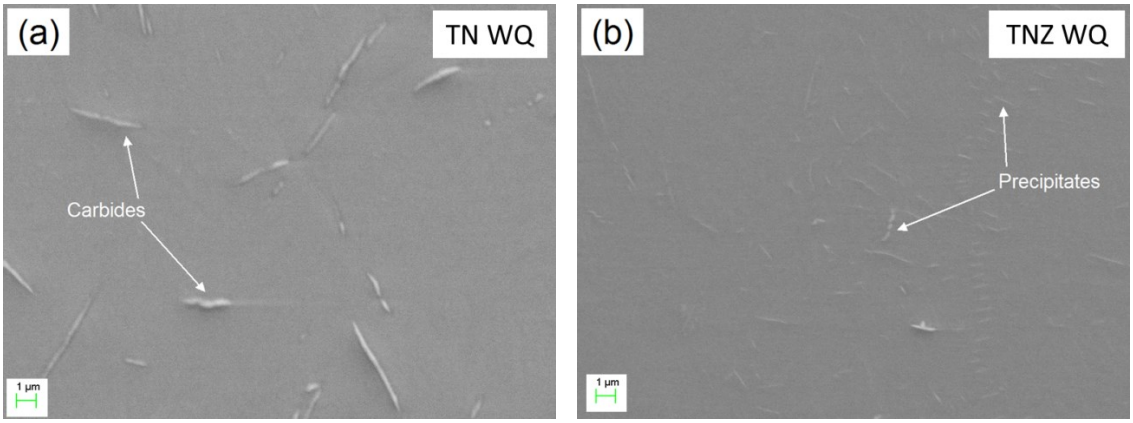

Figure 5.16: SE-images of (a) TN WQ and (b) TNZ WQ

EDS analyses were carried out on the whole α-β structure, α, β and precipitates. All alloys show the same tendencies and, therefore, exemplarily only the results for TN are presented here (Table 5.13, others in Appendix IV). The composition of the whole α-β structure stays stable after the heat treatments. From Table 5.13 (c), it can be seen that the niobium content has decreased in α and increased in β after 1300/650. The same is observed for zirconium (Appendix IV).

The carbide composition is not influenced by the heat treatments. The differing values for carbides in TN WQ are attributable to the accuracy of EDS measurement. They are too small to be analyzed without an overlaying effect from the surrounding matrix.

Table 5.13: EDS analysis of TN standard sintered and after heat treatments in at.%

(a) TN

	α-β structure	α	β	Carbide
Ti	87.2	88.2	85.9	68.8
Nb	12.8	11.8	14.2	2.7
C	n/a	n/a	n/a	28.5

(b) TN 1300

	α-β structure	α	β	Carbide
Ti	88.0	89.9	86.5	69.5
Nb	12.0	10.1	13.5	2.6
C	n/a	n/a	n/a	27.9

(c) TN 1300/650

	α-β structure	α	β	Carbide
Ti	86.9	94.7	80.3	66.8
Nb	13.1	5.3	19.7	2.8
C	n/a	n/a	n/a	30.4

(d) TN WQ

	α-β structure	Carbide
Ti	86.8	71.7
Nb	13.2	11.0
C	n/a	17.3

5.2.4 Grain size measurement

Table 5.14 compares the grain sizes of as-sintered and heat treated samples of TN and TNZ. Due to the high standard deviation, it is not possible to make proper conclusions, but a tendency to slight grain coarsening after heat treating can be observed. The grain size is increasing for both TN and TNZ, where 1300 heat treatment shows the highest values.

Table 5.14: Grain sizes of TN and TNZ before and after heat treating

(a) TN

	Grain size/µm
TN	284 ± 148
TN 1300	315 ± 172
TN 1300/650	299 ± 150

(b) TNZ

	Grain size/µm
TNZ	234 ± 109
TNZ 1300	285 ± 159
TNZ 1300/650	272 ± 130

5.2.5 XRD

TN and TNZ in as-sintered and heat treated condition were analyzed by XRD. The result is shown in Figure 5.17 for TN and in Figure 5.18 for TNZ. The first broad peak that indicates TiO_2 on the surface is also observed after heat treatments. The XRD diffractograms of 1300 and 1300/650 are identical to the as-sintered. Only different peak heights are observed.
In the water quenched TN sample, β and α'' martensite can be indexed, but α is very weak. The diffractogram of the water quenched TNZ specimen shows only peaks associated with β and one weak α peak. Peak broadening is also noticed after thermal treatments.

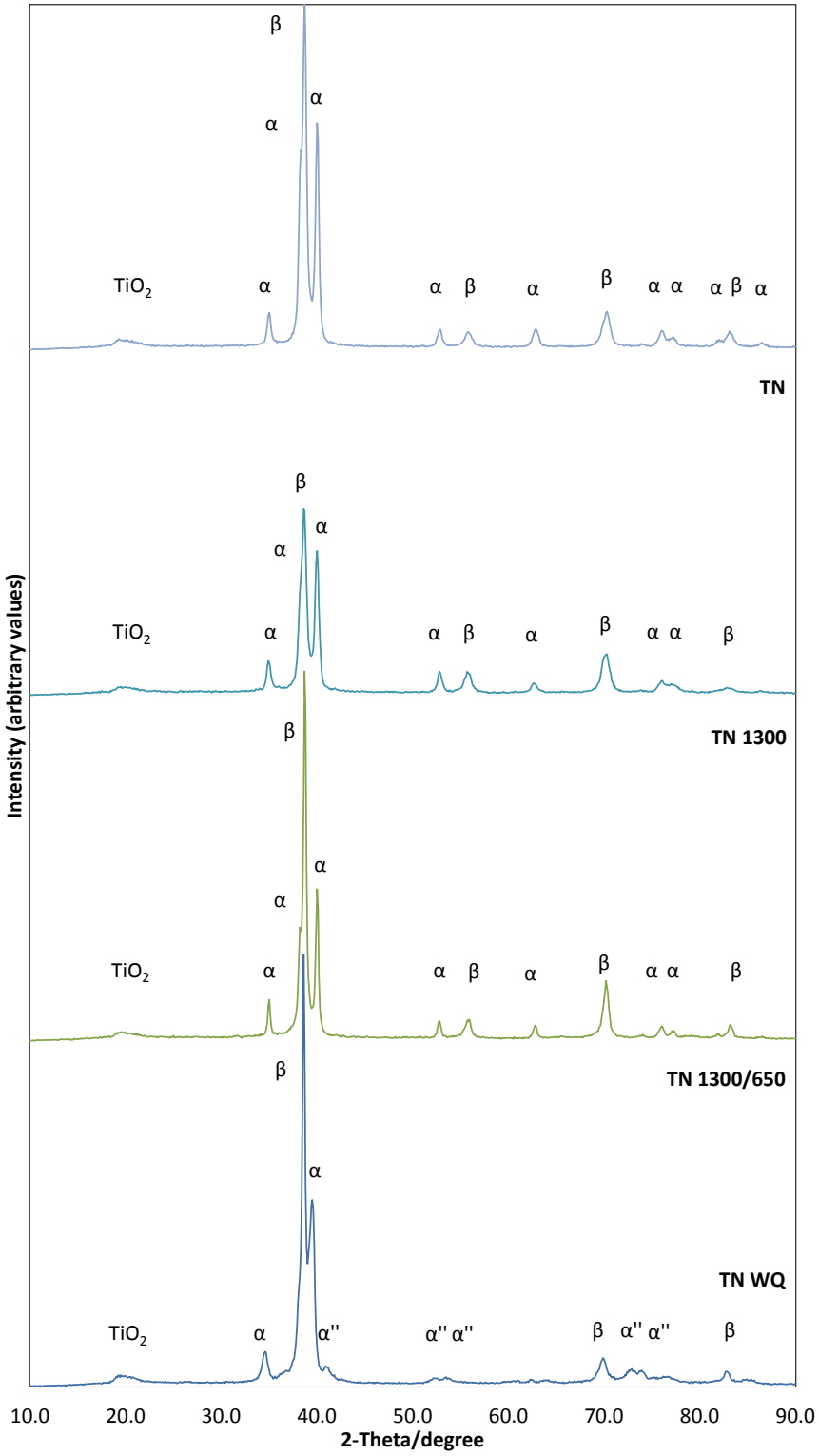

Figure 5.17: XRD diffractograms of TN in as-sintered, 1300, 1300/650 and WQ condition

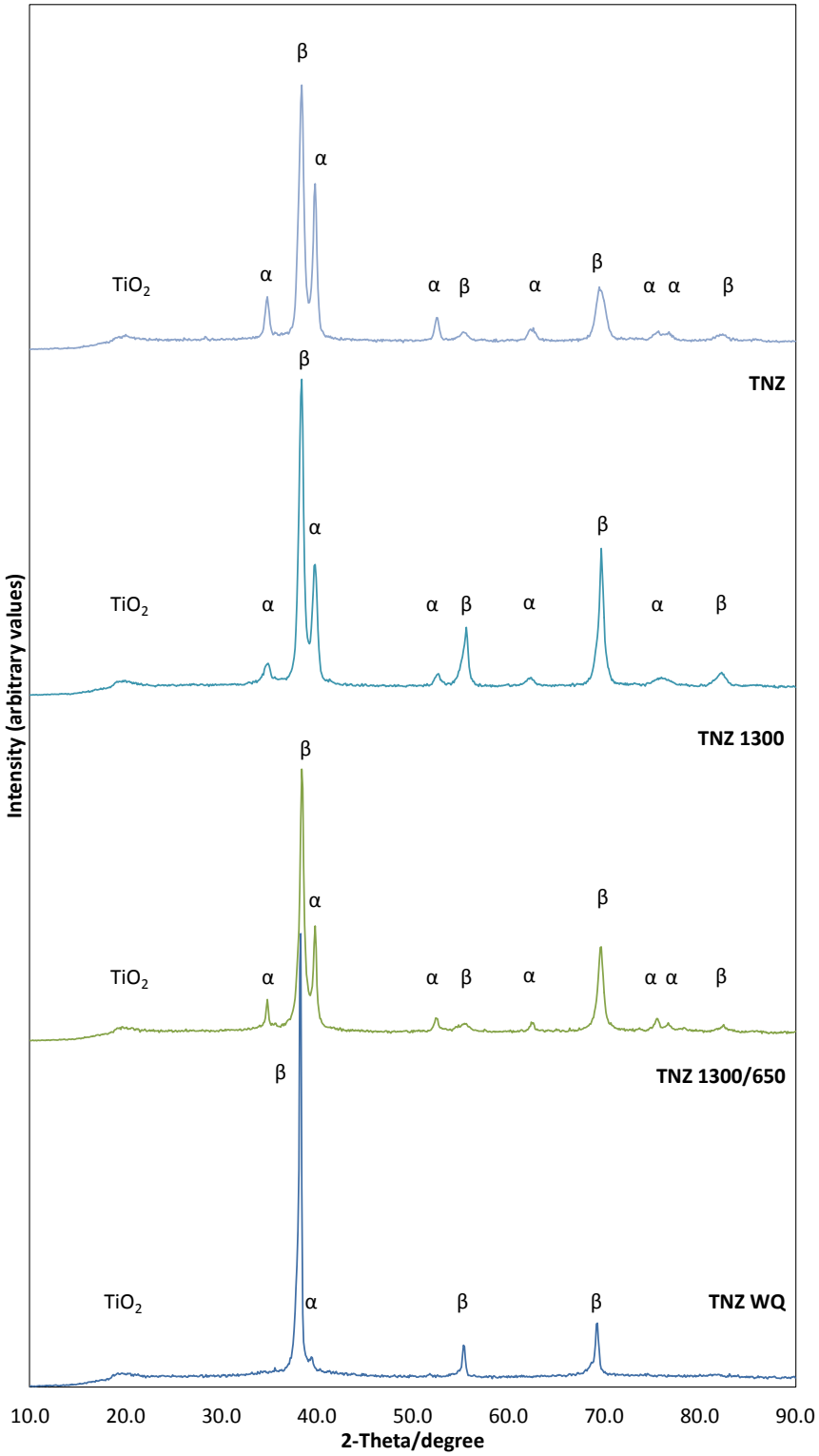

Figure 5.18: XRD diffractograms of TNZ in as-sintered, 1300, 1300/650 and WQ condition

6 Discussion

The discussion is divided in two main parts. In the first part, the results of the as-sintered samples are reviewed and the influence of zirconium and boron addition is analyzed. The effect of the heat treatments is discussed in the second part.

Oxygen and carbon contamination

A big issue in this study was the high amount of oxygen and carbon in the specimens that is exceeding usual values. Final impurity levels that can be achieved in the MIM process of titanium are typically 0.20-0.22 m.% oxygen and 0.04 m.% carbon [20]. Values for MIM Ti-Nb samples in previous works revealed 0.19-0.23 m.% oxygen and 0.04-0.07 m.% carbon [6–8]. In comparison, the chemical analysis of the as-sintered sample (see Figure 5.1) show a O-content of 0.27-0.39 m.% and the C-content varies between 0.06-0.18 m.%.

Every processing step, i.e. the initial powders, process parameters (time, temperature) and environment (binder, atmosphere), contributes to the final amount of interstitials [32]. The influence of the titanium powder can be excluded, because its initial impurity levels have been measured (0.14 m.% oxygen and 0.01 m.% carbon) and they comply with the requirements for grade 1 CP-Ti-powder [33]. The impact of Nb, Zr and B powder can be excluded as they are stored under argon atmosphere and they have also been used by Zhao [6], Beißig [8] and Nagaram [7]. Moreover, the whole powder processing as well as the parameters for debinding and sintering are identical to their work. Hence, it is assumed that the sample contamination was caused by the furnace atmosphere. During thermal debinding, the binder that is extracted from the specimens is evacuated, but some deposits on the bottom and the walls of the furnace. This is usually no problem, because a cleaning cycle is carried out before every sintering. In order to exclude contamination from deposited binder, it has been removed and the sintering plates have been newly coated. Unfortunately, no enhancement was achieved and too high oxygen and carbon contents appeared also in other experiments performed with this furnace. The contamination is probably caused by problems with the pumping system, but this could not be proven so far.

The differences of the impurity levels between standard and fast cooled sintering (see Figure 5.1) were not expected. Beforehand, it was only predicted that fast cooled sintered samples could show lower contamination, because this sintering cycle was shorter and the temperature decreased faster. However, the fluctuations of the impurity levels that are observed in this study can be explained by the number and position of the specimens during sintering (see Figure 4.2). For fast cooled sintering, all 12 specimens were sintered on plate 1. Standard sintering was carried out with 52 samples, but they were divided up on

two plates. TN and TNZ were on plate 1 and TNZxB on plate 2. Experience shows the more samples (i.e. the more material able to getter oxygen) are sintered at the same time in the same container, the less oxygen is picked up per single sample. Therefore, fast cooled samples show higher O-content. The effect of the number of samples is opposite in the case of carbon contamination. TN and TNZ specimens were both times sintered on plate 1, but the higher number of samples during standard sintering results in more binder release and higher C-content. Eventually, the differences in standard sintering occurred, because the specimens have been sintered on two different plates. However, it has to be pointed out, that the effect of the number of samples on O and C uptake is stronger than usual, which can be attributed to the mentioned technical problem of the furnace.

6.1 The as-sintered samples

The specimens in this work were sintered in two different cycles, namely standard sintering and fast cooled sintering. The fast cooled sintering was performed to investigate if an increase of cooling rate in a range technically possible using the given furnace is sufficient to influence the carbide quantity. Zhao [6] reported that the carbides start to precipitate after sintering when the furnace is cooled down. Hence, it was assumed that a higher cooling rate could reduce the precipitation of carbides and, consequently, their quantity. A lower amount of carbides was expected in the fast cooled samples. By comparison of normally and fast cooled samples (Table 5.2 and Table 5.3), different amounts of carbides were observed, but this effect can be attributed to the different C-contents of the samples. For example, the carbide area fraction of standard sintered TN (3.34%) is higher than that of fast cooled sintered TN (2.79%), but also the C-content of standard sintered TN is around 0.07 m.% higher. Therefore, no conclusions concerning the cooling rate after sintering can be made.

The results of all measurements performed on the as-sintered samples are summarized in Table 6.1 for fast cooled sintering and in Table 6.2 and Table 6.3 for standard sintering. At this point, it has to be mentioned that the results of the measurements of quantity of carbides strongly depend on the quality of the images and also on the set threshold as described in chapter 4.3.3 (p. 19). The values vary with slight changes of the threshold and especially small carbide precipitates, like those in TNZxB, were difficult to mark properly. Moreover, the sporadic carbides that were found among the borides were not considered for carbide quantity, because all boride islands were retouched before the calculation.

Table 6.1: Summarized results for the as-sintered samples consolidated by fast cooled sintering

	Chemical analysis m.%		Porosity %		Precipitate quantity area%	
	O-content	C-content	Archimedes'	Image analysis	Carbides	Carbides + Borides
TN	0.32	0.11	4.73	5.18	2.79	-
TNZ	0.33	0.11	5.68	7.30	1.82	-
TNZ3B	0.37	0.12	7.72	9.14	1.22	3.62
TNZ5B	0.39	0.12	8.21	9.58	1.50	3.59

Table 6.2: Summarized results of chemical analysis, porosity and precipitate quantity for the as-sintered samples consolidated by standard sintering

	Chemical analysis m.%		Porosity %		Precipitate quantity area%	
	O-content	C-content	Archimedes'	Image analysis	Carbides	Carbides + Borides
TN	0.27	0.18	4.72	4.72	3.34	-
TNZ	0.28	0.17	5.90	7.28	2.58	-
TNZ3B	0.27	0.06	7.87	9.16	0.82	2.34
TNZ5B	0.30	0.08	8.39	10.33	0.84	3.91

Table 6.3: Summarized results of grain sizes, DSC peak temperatures and phase fractions for the as-sintered samples consolidated by standard sintering

	Grain size/µm	DSC peak temp./°C		Phase fraction/area%	
		Heating	Cooling	α	β
TN	284 ± 148	695	595	67.5	32.5
TNZ	234 ± 109	635	530	52.1	47.9
TNZ3B	168 ± 76	635	533	50.4	49.6
TNZ5B	146 ± 65	650	550	57.4	42.6

6.1.1 Effect of zirconium and boron on α and β

No change of the α-β microstructure was obtained with the addition of zirconium and boron. The typical basket weave structure of α and β lamellae is present in all as-sintered samples (see e.g. Figure 5.4). With regard to previous works [6-8], α phase correlates with black lamellae and β phase with white lamellae.

Zirconium shows complete solubility in α and β (Table 5.4), which is in accordance with the Ti-Zr phase diagram [34]. Compared to the weighed portion at powder mixing, the measured values for zirconium appear slightly too high (around 7.5 at.% instead of 6 at.%). This difference probably occurs, because the Lα peaks of zirconium and niobium are overlapping and could not be distinguished properly by the software. To avoid this problem, other peaks of Nb and Zr could be excited by a higher accelerating voltage. However, this would also cause an increase of the analytical area and might lead to problems with the detection of lighter elements like boron and carbon. Hence, in this study only a qualitative and comparing observation of the collected EDS spectra is done, because the quantification results can be affected by various factors (e.g. background fitting, used standards, overlapping peaks) [35].

The EDS results revealed also almost the same content of niobium in both α and β of around 13 at.% (Table 5.4). In contrast to that, the Ti-Nb phase diagram [36] predicts a limited solubility in α of 2.0-2.5 at.% at a temperature between 600 °C and 650 °C. The high amount of niobium in α can be an indication that there was not enough time for niobium to distribute properly when the samples were cooled down after sintering. Niobium is like aluminum and molybdenum a slow diffusion element in titanium [9]. A good review of the diffusion of interstitial and substitutional elements in titanium can be found in Zwicker [37]. A better distribution of niobium is achievable by heat treatments, as it can be seen e.g. in Table 5.13. The Nb-content in the α-phase is decreasing from 11.8 at.% to 5.3 at.% after 1300/650 heat treatment.

XRD

The XRD diffractograms of TN and TNZ (Figure 5.8) confirm that the alloys consist of α and β phase. Rietveld method would be necessary for an accurate determination of the α/β ratio, but this was not performed in this work. The observed peak broadening is called Lorentz broadening or microstress-broadening and is caused by stress in the material. This stress has probably been induced during the grinding of the surface that was done before the measurement [38]. Furthermore, the XRD diffractograms of the water quenched TN samples (Figure 5.17) indicate the formation of martensitic α'', which was expected. It will be discussed later in chapter 6.2.3 (p. 54).

The TiO_2 peak that was observed in all XRD diffractograms (Figure 5.8, Figure 5.17 and Figure 5.18) is an evidence for the high affinity of titanium to oxygen. As soon as titanium is exposed to air, titanium oxides are formed on the surface [9, 38].

The addition of zirconium is increasing the lattice parameters of titanium, which can be seen from the shift of the TNZ diffractogram to smaller angles (Figure 5.8). This effect was also investigated by Nagaram [7] and can be attributed to the higher atomic radius of zirconium (1.60 Å) compared to titanium (1.45 Å) [39]. Figures that illustrate the influence of different elements on the lattice parameters of titanium can be found, for example, in Zwicker [37].

DSC

The peak in the DSC curves (A-D in Figure 5.9, H-K in Figure 5.10) occurs for all samples and correlates to the α-β transformation. The other peaks that are found for TN and TNZ3B in the heating curves (E-G in Figure 5.9) as well as the decreased slope about 1000 °C in the cooling curves (Figure 5.10) could indicate the beginning of carbide dissolution and precipitation. An accurate evaluation of the curves is limited because the signals are rather weak. To get sharper peaks, DSC measurements should be performed with a lower cooling rate as it was done by Zhou *et al.* [40]. Alternatively, dilatometry could be performed. Gasik *et al.* [41] performed thermal analysis of Ti-13Nb-13Zr (m.%). They reported that dilatometric measurements are advantageous if transformations have a low heat release or are spread over a wide temperature range, which is difficult to measure with DSC. A better characterization of the α-β transformation could be possible, but carbide formation is not detectable with this method.

Thus, a determination of the β transus temperature from the DSC measurements is not reliable, but a comparison of the peak positions is possible, because all measurements were performed with the same parameters. The addition of zirconium and boron is influencing the α-β transformation peak. This can be clearly seen from the heating and cooling curves (Figure 5.9 and Figure 5.10) and from the peak temperatures that are summarized in Table 6.3. Compared to TN, the peak of TNZ is shifted to lower temperatures and the peak temperature decreases. This can be explained by the β-stabilizing effect of zirconium that is also observed in other publications [11, 40]. The peak temperature for TNZxB is also lower than that of TN, but slightly higher than for TNZ. TNZxB contains not only zirconium as β stabilizer, but also boron, which is stabilizing the α phase [10]. Both effects are reflected in the DSC results and they are also visible in the results of the α and β phase fractions (Table 5.12). The α phase fraction of the as-sintered samples is decreasing from around 68% in TN to around 50% in TNZ and TNZ3B and slightly increasing again to around 57% for

TNZ5B. However, the inaccuracy of the phase fraction determination has to be considered, because only one image of each composition was used for the calculation.

6.1.2 Effect of zirconium and boron on precipitation in Ti-22Nb

The formation of titanium carbides that precipitate preferentially at grain boundaries is observed in all alloys (see e.g. Figure 5.2). The quantity of carbides could be reduced by adding zirconium and boron (Table 5.3), as it was already reported by Beißig [8] and Nagaram [7].

The addition of zirconium leads to a decrease of the carbide quantity (Table 5.3). In both TN and TNZ the C-content amounts to 0.11 m.%, but the carbide area fraction decreases from 2.79% for TN to 1.82% for TNZ. Considering the XRD results (Figure 5.8), the substitution of Nb atoms by Zr atoms causes an increase of the lattice parameters. Consequently, the carbon solubility is increased and less carbides precipitate.

Boron addition to TNZ results in further carbide reduction (Table 5.3) and the formation of borides (see e.g. Figure 5.2 (c), (d)). The carbide area fraction was determined as 1.22% for TNZ3B and 1.50% for TNZ5B, where the higher value for TNZ5B is probably caused by the higher carbon content that was measured in TNZ5B. The reason for the carbide reduction by boron addition could not be determined with the methods used in this work. Possible reasons are the formation of precipitates that are not visible with SEM or an increase of carbon solubility. With regard to Table 5.12, the addition of boron could increase the α phase fraction and, consequently, the solubility of carbon. The maximal solubility of carbon is given as 2.0 at.% in α and 0.55 at.% in β [37].

Both zirconium and boron showed good results with regard to carbide reduction. It is assumed by Beißig [8] and Nagaram [7] that new compounds of precipitates and small precipitates are formed when boron or zirconium is added to Ti-Nb alloys, but this could not be proven so far. Therefore, future investigations with e.g. transmission electron microscopy (TEM) have to be performed.

Borides

The addition of 0.3 and 0.5 m.% boron to Ti-22Nb-10Zr led to the formation of boride islands with varying amount of niobium (Figure 5.6, Table 5.5). Based on the work of Beißig [8] and previous publications [42, 43], these borides are assumed to be TiB with niobium enrichment.

Ferri [44] studied the precipitation of TiB in Ti-6Al-4V-0.5B. From dilatometry experiments, he stated that the titanium borides are formed around 800 °C during the sintering process.

Furthermore, this author reported the advantage of MIM for a homogenous boride distribution, but boride accumulations are observed in this work. This indicates on the one hand that the boron particles are not well distributed in the feedstock. On the other hand, the diffusion of boron atoms seems to be strongly limited during sintering. This limitation is probably caused by niobium particles. Zhao [6] reported that the diffusion of niobium during sintering starts above 900 °C. At lower temperatures, niobium acts as a diffusion barrier for other elements. According to the Ti-B phase diagram [45], the solubility of boron in α- and β-Ti is limited (<1 at.%). Unfortunately, studies about the diffusion of boron in β-titanium are lacking, but boron is stated as ultra-fast diffuser in α-titanium [46]. Thus, it is assumed that boron is not able to distribute homogenously due to niobium, and boride islands are formed as a consequence.

To overcome this problem, an optimization of the mixing technique is necessary to ensure a good homogenization of the feedstock. Another alternative could be the use of pre-alloyed powder or master alloys instead of elemental powders.

6.1.3 Effect of zirconium and boron on porosity

It can be seen from Table 5.1, that the porosity of standard and fast cooled sintered samples is similar. The difference between Archimedes' porosity and image analysis occurs due to open and closed porosity. If there are open pores in the specimen, the porosity calculation based on Archimedes' principle is falsified, because the ethanol can enter the part and a higher density is measured [47].

The increase of porosity in TNZ and TNZxB reveals that zirconium and boron have a significant effect on sintering. The sintering process of Ti-Nb alloys was intensely investigated by Zhao [6]. At lower temperatures, only diffusion of titanium takes place and bigger niobium particles act as diffusion barriers. The homogenization process of Ti-Nb starts above 900 °C and is dominated by unidirectional diffusion from Nb to Ti due to their different diffusion coefficients. Zirconium, as a third alloying element, and the formation of borides contribute to a further inhibition of the diffusion processes. Higher porosity was measured as a consequence.

To enhance densification, attempts for a better feedstock homogenization or the use of pre-alloyed powder, as it is mentioned before, could be useful.

6.1.4 Effect of zirconium and boron on grain size

The grain refinement with addition of Zr and B (Table 5.6) can be attributed to decelerated diffusion processes during sintering also observed by Ferri [44], Beißig [8] and Nagaram [7]. An additional mechanism preventing grain coarsening during sintering is the pinning of grain boundaries with elements or particles [22]. In this case, borides and zirconium could pin the grain boundaries. Cherukuri *et al.* [48] reported that TiB, which precipitates at grain boundaries, leads to a restriction of grain growth in the β-titanium alloy Ti–15Mo–2.6Nb–3Al–0.2Si (m.%) by Zener pinning. A reduction of the grain boundary mobility by TiB is also predicted by Tamirisakandala *et al.* [50, 51], but studies about a possible pinning effect of zirconium in titanium are lacking. As long as the carbon content does not exceed the solubility at 1300 °C, no carbides should be present during sintering, so they do not contribute to grain growth hindering. They are formed during cooling [6]. German [49] reported that grain coarsening and densification are strongly connected during sintering. Smaller grain size is observed when the porosity is increasing, because pores that are lying on grain boundaries also contribute to the pinning effect. Thus, the higher porosity in TNZ and TNZxB is preventing excessive grain growth.

6.2 Effect of heat treatments

Heat treatments of TN, TNZ and TNZxB were carried out aiming a decrease of the number of carbide precipitates. To consider a possible influence of oxygen and carbon pickup during thermal cycles, the oxygen and carbon content has been analyzed after the 1300 and 1300/650 heat treatments. The results are shown in Table 5.7 to Table 5.10. The differences are marginal and, hence, are neglected in the following discussion.

As already mentioned, contamination of the samples was higher than the typical values. This has to be considered when discussing the effect of the heat treatments. Therefore, the calculated Ti-22Nb – C phase diagram is depicted again at this point (Figure 6.1). Temperatures used for heat treatments (1300 °C and 650 °C) are marked with horizontal lines. The measured C-content of the MIM samples produced by Zhao [6] is defined with the blue shaded area. The vertical lines mark the respective C-contents of the as-sintered specimens observed in this work (Figure 5.1). The further discussion is based on this phase diagram, but it has to be mentioned that it was calculated without considering zirconium and boron. Moreover, a possible influence of oxygen that is acting as α-stabilizer [9] is also not considered within the calculation. Thus, changes of the phase diagram that are probably caused by these elements are not known in this study, but they cannot be excluded.

TNZxB samples exhibit carbon values similar to those fabricated by Zhao and full carbide dissolution can be expected at 1300 °C. At 650 °C, dissolution of carbides can also be expected for TNZ5B, but it is questionable for TNZ3B, because the carbon value is close to the solubility limit. According to the phase diagram, carbides in TN and TNZ are not dissolved at 650 °C. Both alloys are around the solubility line at 1300 °C and carbides possibly cannot dissolve completely. This could explain why no significant grain coarsening was observed for these alloys (Table 5.14), because residual carbides can pin the grain boundaries and avoid grain growth.

According to Witusiewicz *et al.* [52], borides are stable in the temperature range used in this study. Therefore, no phase change of the borides is expected. Based on the results of the precipitate quantity (Table 5.11) it is not possible to make reliable conclusions about the formation or dissolution of borides during the heat treatments. The evaluation of more images is necessary to obtain more accurate results of the precipitate quantity.

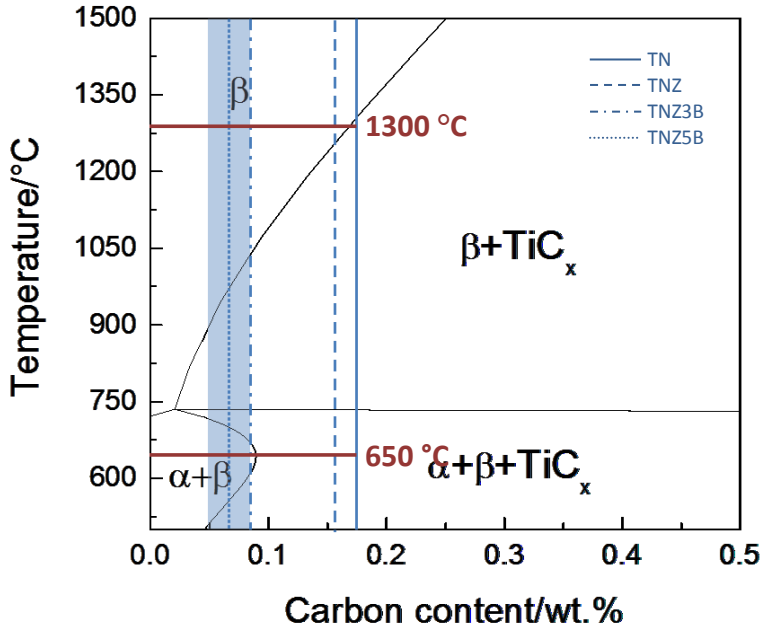

Figure 6.1: Calculated Ti-22Nb – C phase diagram with indication of the two main temperatures used for heat treatments (1300 °C and 650 °C). The blue shaded area marks the C-content of the MIM samples produced by Zhao [31]. The vertical lines mark the respective C-content of the as-sintered MIM samples produced in this work.

A summary of the results obtained from heat treating is given in Table 6.4 to Table 6.7.

Table 6.4: Summarized results for standard sintered and heat treated TN

TN	O-content m.%	C-content m.%	Carbide quant. area%	Grain size µm	Phases	α/β ratio area%	
						α	β
As-sintered	0.27	0.18	3.34	284 ± 148	α + β	67.5	32.5
1300	0.30	0.18	3.85	315 ± 172	α + β	65.3	34.7
1300/650	0.29	0.18	2.70	299 ± 150	α + β	60.1	39.9
WQ	n/a	n/a	n/a	n/a	β + α''	n/a	n/a

Table 6.5: Summarized results for standard sintered and heat treated TNZ

TNZ	O-content m.%	C-content m.%	Carbide quant. area%	Grain size µm	Phases	α/β ratio area%	
						α	β
As-sintered	0.28	0.16	2.58	234 ± 109	α + β	52.1	47.9
1300	0.29	0.16	2.64	285 ± 159	α + β	50.1	49.9
1300/650	0.27	0.14	2.44	272 ± 130	α + β	22.7	77.3
WQ	n/a	n/a	n/a	n/a	β	n/a	n/a

Table 6.6: Summarized results for standard sintered and heat treated TNZ3B

TNZ3B	O-content m.%	C-content m.%	Precipitate quantity area%		α/β ratio area%	
			Carbides	Carbides + Borides	α	β
As-sintered	0.27	0.06	0.86	2.34	50.4	49.6
1300	0.28	0.08	1.08	2.91	55.5	44.5
1300/650	0.27	0.06	0.80	2.23	33.5	66.5
WQ	n/a	n/a	n/a	2.09	n/a	n/a

Table 6.7: Summarized results for standard sintered and heat treated TNZ5B

TNZ5B	O-content m.%	C-content m.%	Precipitate quantity area%		α/β ratio area%	
			Carbides	Carbides + Borides	α	β
As-sintered	0.30	0.08	0.84	3.91	57.4	42.6
1300	0.30	0.08	0.87	3.10	53.2	46.8
1300/650	0.30	0.08	0.68	2.42	35.5	64.5
WQ	n/a	n/a	n/a	2.45	n/a	n/a

6.2.1 1300

The 1300 heat treatment was carried out for 2 h at 1300 °C followed by fast cooling to room temperature. The determination of carbide quantity reveals that instead of carbide reduction, the amount of carbides tends to increase (Table 5.11). It seems that a re-heating to 1300 °C favors the further precipitation of carbides. The cooling rate was higher for 1300 heat treatment than for standard sintering and a decrease of the carbide quantity was expected. For TN and TNZ, the thermal cycle is performed around the solubility line and not in the pure β region. This can explain the higher carbide quantity, because carbides had additional time to precipitate during the dwell time of 2 h. The reason for the higher carbide quantity in TNZxB is not clear. At 1300 °C, carbides are predicted to be fully dissolved and the re-precipitation should be reduced by fast cooling. However, it has to be taken into account that the higher values can also be attributed to measuring inaccuracy as it is discussed earlier.

6.2.2 1300/650

The 1300/650 heat treatment shows a remarkable effect on the basket weave microstructure as it can be seen for example in Figure 5.14 (c) for TN. The size of α lamellae is increasing from 0.2-0.6 µm to 1-2 µm. This growth occurred during the dwell time in the (α+β) region at 650 °C, where α-phase had time to coarsen by diffusion. The very fine lamellar structure that can be seen in the β phase is secondary α that forms during the final cooling to room temperature [9]. When comparing the BSE-images of TN (Figure 5.14) with those of TNZ (Figure 5.15) and TNZxB (Appendix III), it can be seen that the bright areas, which represent β phase, are bigger in TNZ and TNZxB. The higher amount of β phase in TNZ and TNZxB can also be seen from Table 5.12. The β phase fraction in the 1300/650 heat treated samples is increasing from 40% in TN to around 77% in TNZ, 67% in TNZ3B and 65%

TNZ5B, which confirms the β-stabilizing effect of zirconium. The decrease of the β phase fraction with addition of boron can be attributed to the α-stabilizing effect of this element. As already mentioned before, only tendencies can be observed from the phase fraction analysis. The evaluation of more images is necessary for proper conclusions.

The EDS measurements after the heat treatments (see e.g. Table 5.13) show that the composition of α and β has changed. In the as-sintered samples, niobium was equally distributed, but a depletion of niobium in α is observed in the heat treated samples. It can be assumed that during the holding step at 650 °C niobium had time to diffuse, so the alpha phase depletes as predicted by the Ti-Nb phase diagram [36]. Thus, the size of the analytical area has to be considered, because the lamellar structure in the as-sintered condition is probably too fine for an analyzation of the single lamellae, while the thicker lamellae in the heat treated condition could be analyzed separately.

A decrease of the carbide quantity by this heat treatment could be achieved in all compositions (Table 5.11). The results for TNZxB demonstrate that it is possible to exploit the regions of increased carbide solubility below the β transus temperature for carbide reduction. The carbides are partially or completely dissolved in the carbide-free zone and less carbides precipitate during subsequent cooling.

The reason for the lower carbide quantity of TN and TNZ and the thinner shape of the carbides is not clear. According to the phase diagram, the C-content is too high for dissolution of the carbides. However, it has to be taken into account that the phase diagram only reflects the equilibrium state of Ti-22Nb with C without considering zirconium and, in fact, a possible dissolution of carbides cannot be excluded.

6.2.3 WQ

In terms of carbide reduction, the best results were achieved by water quenching. The carbide precipitation is completely suppressed in TNZxB. Only the boride islands are visible with optical microscope and SEM (see e.g. Figure 5.13 (d)). With regard to the calculated Ti-22Nb – C phase diagram (Figure 6.1), the carbides in TN and TNZ are not fully dissolved at 1300 °C and thus, they cannot be avoided completely.

Besides, a change of the phases is observed only after water quenching. With regard to the XRD diffractograms (Figure 5.17 and Figure 5.18), α and β stay unchanged after 1300 and 1300/650 heat treatment. Water quenching leads to the co-existence of β phase and the martensitic α'' phase in TN (Figure 5.17). The formation of α'' instead of α' was expected, because β-stabilizing elements favor α'' phase. The α'/α'' martensite boundary in the binary Ti-Nb system is stated as 5.7 at.% [9].

Zirconium suppresses the formation of α'' phase after water quenching and, thus, only peaks associated with β are detected (Figure 5.18). Kim *et al.* [53] reported that the martensitic start temperature decreases by 38 K with addition of 1 at.% zirconium to Ti-22Nb.

In summary, the heat treatments were performed in order to reduce the carbide quantity, but this was not achieved by all chosen thermal cycles. A heat treatment in the carbide-free region at high temperatures is only successful if the cooling rate is high enough to prevent re-precipitation as it was demonstrated by water quenching.
The 1300/650 heat treatment of TNZxB showed that carbides can be reduced by exploiting their solubility in the (α+β) region. However, this kind of heat treatment should be repeated with different cooling rates to gain more meaningful results. Moreover, the calculation of phase diagrams including zirconium and boron would be helpful.

7 Summary and outlook

Metal injection molding (MIM) was used to process four different Ti-Nb alloys, namely Ti-22Nb, Ti-22Nb-10Zr, Ti-22Nb-10Zr-0.3B, and Ti-22Nb-10Zr-0.5B (all m.%). Three different heat treatments were performed: (1) 2 h at 1300 °C and fast cooling, (2) 2 h at 1300 °C, 10 h at 650 °C and fast cooling, and (3) 10 min at 1300 °C and water quenching.
Microstructure of as-sintered and heat treated samples was analyzed by optical microscopy, SEM and EDS. Oxygen and carbon content were measured. Porosity and precipitate area fraction was determined. Images retained from EBSD measurements were used to calculate the grain size. Furthermore, XRD diffractograms and DSC curves were generated to observe phase changes.

The results and analysis obtained in this work lead to the following conclusions:

- The addition of 10 m.% zirconium to Ti-22Nb leads to significant carbide reduction. The reason is an increase of the lattice parameters that is enhancing the carbon solubility. Furthermore, zirconium is influencing the diffusion processes during sintering. Consequently, higher porosity and grain refinement is observed. It is also shown that zirconium is stabilizing the β phase and suppressing the formation of α'' martensite.

- The addition of 0.3 and 0.5 m.% boron to Ti-22Nb-10Zr effected the formation of boride islands. The borides are identified as TiB with niobium enrichment. An increase in porosity and a decrease in grain size are also observed. Higher porosity, grain refinement and the inhomogeneous distribution of borides are attributed to the influence of boron on the sintering process. Moreover, the amount of carbide precipitates can be reduced with boron addition, but the reason for this effect stays unanswered. An increase in carbon solubility or the formation of other precipitates that are not visible with SEM might be possible.

- A reduction of carbide precipitates exploiting the solubility area in the β region is only successful, if the cooling rate is high enough to suppress a re-precipitation of carbides. A cooling rate of 75 K/min, as it was performed by 1300 heat treatment (1), is insufficient and the carbide quantity is even increasing. Subsequent water quenching (3) suppressed carbide precipitation and presents the most promising thermal treatment.

- The heat treatment in the solubility area in the (α+β) region (2) could decrease carbide precipitates in all compositions. While the carbide reduction in Ti-22Nb-10Zr-0.3B and Ti-22Nb-10Zr-0.5B is in accordance with the dwell time in the solubility area, the reason for carbide reduction in Ti-22Nb and Ti-22Nb-10Zr is not clear.

In summary, it could be shown in this work that carbide precipitates in Ti-22Nb alloys processed by MIM can be reduced by the addition of zirconium and boron and by suitable heat treatments. TEM investigations should be performed for a more accurate identification of the precipitates. The detrimental effect of zirconium and boron on the sintering process might be avoided by optimization of the sintering parameters. Alternatively, pre-alloyed powders or master alloy powders should be used instead of elemental powders. This might probably also lead to a better distribution of borides.

The Ti-22Nb – C phase diagram, which was used as a reference in this study, was calculated without considering zirconium or boron, but changes in the phase diagram caused by the addition of these elements cannot be excluded. The calculation of phase diagrams including boron and zirconium would be helpful to choose appropriate heat treatments.

Furthermore, heat treatments are influencing the microstructure and consequently, the mechanical properties. Therefore, further heat treatments and an evaluation of the mechanical properties should be performed in future studies.

References

1. M. Geetha, A. K. Singh, R. Asokamani, and A. K. Gogia, “Ti based biomaterials, the ultimate choice for orthopaedic implants–a review,” Progress in Materials Science **54**, 397–425 (2009).
2. E. Wintermantel and S.-W. Ha, *Medizintechnik: Life Science Engineering* (Springer-Verlag, 2008).
3. J. Breme, E. Eisenbarth, and V. Biehl, “Titanium and its alloys for medical applications,” in *Titanium and titanium alloys*, C. Leyens and M. Peters, eds. (WILEY-VCH Verlag GmbH & Co. KGaA, 2003), pp. 423–451.
4. M. Long and H. J. Rack, “Titanium alloys in total joint replacement—a materials science perspective,” Biomaterials **19**, 1621–1639 (1998).
5. T. Ebel, “Metal injection moulding (MIM) of titanium and titanium alloys,” in *Handbook of Metal Injection Moulding*, D. F. Heaney, ed. (Woodhead Publishing Ltd, 2012), pp. 415–445.
6. D. Zhao, *Metal Injection Moulding of Titanium-Niobium Alloys for Biomedical Applications*, Dissertation, BTU Cottbus, 2014.
7. A. B. Nagaram, *Effect of Zr-addition on carbide precipitation in Ti-Nb processed by Metal Injection Moulding*, Master Thesis, TU Darmstadt, 2015.
8. T. Beißig, *Karbidausscheidungen bei β-Titanlegierungen im MIM-Prozess*, Master Thesis, TU Berlin, 2015.
9. G. Lütjering and J. C. Williams, *Titanium* (Springer-Verlag, 2003).
10. M. Peters, J. Hemptenmacher, J. Kumpfert, and C. Leyens, “Structure and Properties of Titanium and Titanium Alloys,” in *Titanium and titanium alloys*, C. Leyens and M. Peters, eds. (WILEY-VCH Verlag GmbH & Co. KGaA, 2003), pp. 1–36.
11. M. Abdel-Hady, H. Fuwa, K. Hinoshita, H. Kimura, Y. Shinzato, and M. Morinaga, “Phase stability change with Zr content in β-type Ti–Nb alloys,” Scripta Materialia **57**, 1000–1003 (2007).
12. A. Biesiekierski, J. Wang, M. A.-H. Gepreel, and C. Wen, “A new look at biomedical Ti-based shape memory alloys,” Acta biomaterialia **8**, 1661–1669 (2012).
13. A. Cremasco, A. D. Messias, A. R. Esposito, de Rezende Duek, Eliana Aparecida, and R. Caram, “Effects of alloying elements on the cytotoxic response of titanium alloys,” Materials Science and Engineering: C **31**, 833–839 (2011).
14. E. Eisenbarth, D. Velten, M. Müller, R. Thull, and J. Breme, “Biocompatibility of β-stabilizing elements of titanium alloys,” Biomaterials **25**, 5705–5713 (2004).

15. K. Wang, “The use of titanium for medical applications in the USA,” Materials Science and Engineering: A **213**, 134–137 (1996).
16. R. M. German, “Metal powder injection molding (MIM): key trends and markets,” in *Handbook of Metal Injection Moulding*, D. F. Heaney, ed. (Woodhead Publishing Ltd, 2012), pp. 1–25.
17. D. F. Heaney, ed., *Handbook of Metal Injection Moulding* (Woodhead Publishing Ltd, 2012).
18. I. Todd and A. T. Sidambe, “Developments in metal injection moulding (MIM),” in *Advances in powder metallurgy*. *Properties, processing and applications*, I. Chang and Y. Zhao, eds. (Woodhead Publishing Ltd Cambridge, 2013), pp. 109–146.
19. R. M. German, *Powder injection molding* (Metal Powders Industries Federation, 1990).
20. R. M. German, “Progress in titanium metal powder injection molding,” Materials **6**, 3641–3662 (2013).
21. W. Schatt, *Sintervorgänge: Grundlagen* (VDI-Verlag, 1992).
22. R. M. German, *Sintering Theory and Practice* (John Wiley & Sons, Inc., 1996).
23. R. Simon, *Technologie Keramischer Werkstoffe (410.015)*. *10. Sintern - Transportmechanismen* (SS 2011).
24. R. German, “Titanium powder injection moulding: a review of the current status of materials, processing, properties and applications,” Powder Injection Moulding International **3**, 21–37 (2009).
25. A. T. Sidambe, “Biocompatibility of advanced manufactured titanium implants—A review,” Materials **7**, 8168–8188 (2014).
26. J. Lincks, B. D. Boyan, C. R. Blanchard, C. H. Lohmann, Y. Liu, D. L. Cochran, D. D. Dean, and Z. Schwartz, “Response of MG63 osteoblast-like cells to titanium and titanium alloy is dependent on surface roughness and composition,” Biomaterials **19**, 2219–2232 (1998).
27. D. D. Deligianni, N. Katsala, S. Ladas, D. Sotiropoulou, J. Amedee, and Y. F. Missirlis, “Effect of surface roughness of the titanium alloy Ti–6Al–4V on human bone marrow cell response and on protein adsorption,” Biomaterials **22**, 1241–1251 (2001).
28. J.-E. Bidaux, C. Closuit, M. Rodriguez-Arbaizar, D. Zufferey, and E. Carreño-Morelli, “Metal injection moulding of low modulus Ti-Nb alloys for biomedical applications,” Powder Metallurgy **56**, 263–266 (2013).
29. J. E. Bidaux, C. Closuit, M. Rodriguez-Arbaizar, and E. Carreno-Morelli, “Metal injection moulding of Ti-Nb alloys for implant application,” European Cells and Materials **22**, 32 (2011).

30. M. Yan, M. Qian, C. Kong, and M. S. Dargusch, “Impacts of trace carbon on the microstructure of as-sintered biomedical Ti–15Mo alloy and reassessment of the maximum carbon limit,” Acta biomaterialia **10**, 1014–1023 (2014).
31. D. Zhao, K. Chang, T. Ebel, M. Qian, R. Willumeit, M. Yan, and F. Pyczak, “Titanium carbide precipitation in Ti-22Nb alloy fabricated by metal injection moulding,” Powder Metallurgy **57**, 2–4 (2014).
32. E. Baril, L. P. Lefebvre, and Y. Thomas, “Interstitials Sources and Control in Titanium P/M Process,” PM2010 Powder Metallurgy World Congress, 219–226 (2010).
33. ASTM, *B348-02* .
34. J. L. Murray, “The Ti− Zr (Titanium-Zirconium) system,” Bulletin of Alloy Phase Diagrams **2**, 197–201 (1981).
35. M. Dr. Oehring and U. Lorenz, HZG (personal communication, 2016).
36. J. L. Murray, “The Nb− Ti (Niobium-Titanium) system,” Bulletin of Alloy Phase Diagrams **2**, 55–61 (1981).
37. U. Zwicker, *Titan und titanlegierungen* (Springer-Verlag, 2013).
38. D. Dr.rer.nat. Höche, HZG (personal communication, 2016).
39. M. Gliech, “Rutherford Lexikon der Elemente - Atomradien,” http:// www.uniterra.de/rutherford/index.html, March 2016.
40. Y. Zhou, Y. Li, X. Yang, Z. Cui, and S. Zhu, “Influence of Zr content on phase transformation, microstructure and mechanical properties of Ti 75− x Nb 25 Zr x (x= 0–6) alloys,” Journal of Alloys and Compounds **486**, 628–632 (2009).
41. M. M. Gasik and H. Yu, “Phase Equilibria and Thermal Behavior of the Biomedical Ti-Nb-Zr Alloy,” 17th Plansee Seminar, RM 29/1 (2009).
42. S. Nag, S. Samuel, A. Puthucode, and R. Banerjee, “Characterization of novel borides in Ti–Nb–Zr–Ta+ 2B metal-matrix composites,” Materials characterization **60**, 106–113 (2009).
43. H. Feng, Y. Zhou, D. Jia, Q. Meng, and J. Rao, “Growth mechanism of in situ TiB whiskers in spark plasma sintered TiB/Ti metal matrix composites,” Crystal growth & design **6**, 1626–1630 (2006).
44. O. M. Ferri, *Optimisation of Fatigue Behaviour of Ti-6Al-4V Alloy Components Fabricated by Metal Injection Moulding*, Dissertation, TU Hamburg-Harburg, 2010.
45. J. L. Murray, P. K. Liao, and K. E. Spear, “The B− Ti (Boron-Titanium) system,” Bulletin of Alloy Phase Diagrams **7**, 550–555 (1986).
46. S. V. Divinski, F. Hisker, T. Wilger, M. Friesel, and C. Herzig, “Tracer diffusion of boron in α-Ti and γ-TiAl,” Intermetallics **16**, 148–155 (2008).

47. W. Schatt and K.-P. Wieters, *Powder metallurgy: processing and materials* (European Powder Metallurgy Association EPMA, 1997).
48. B. Cherukuri, R. Srinivasan, S. Tamirisakandala, and D. B. Miracle, “The influence of trace boron addition on grain growth kinetics of the beta phase in the beta titanium alloy Ti–15Mo–2.6 Nb–3Al–0.2 Si,” Scripta Materialia **60**, 496–499 (2009).
49. R. M. German, “Coarsening during Sintering,” PM2010 World Congress - Sintering: Fundamentals and Modelling, 49–56 (2010).
50. S. Tamirisakandala, R. B. Bhat, J. S. Tiley, and D. B. Miracle, “Processing, microstructure, and properties of β titanium alloys modified with boron,” Journal of materials engineering and performance **14**, 741–746 (2005).
51. S. Tamirisakandala, R. B. Bhat, J. S. Tiley, and D. B. Miracle, “Grain refinement of cast titanium alloys via trace boron addition,” Scripta Materialia **53**, 1421–1426 (2005).
52. V. T. WITUSIEWICZ, A. A. BONDAR, U. HECHT, S. REX, and T. Y. VELIKANOVA, “The Al-B-Nb-Ti system II. Thermodynamic description of the constituent ternary system B-Nb-Ti,” Journal of Alloys and Compounds **456**, 143–150 (2008).
53. J. I. Kim, H. Y. Kim, T. Inamura, H. Hosoda, and S. Miyazaki, “Shape memory characteristics of Ti–22Nb–(2–8) Zr (at.%) biomedical alloys,” Materials Science and Engineering: A **403**, 334–339 (2005).

Appendix

Appendix I – List of samples

App. Table 1: List of samples produced in this work

Material	Sample name	Cooling after sintering	Heat treatment
Ti-22Nb	TN	10 K/min	
	TN 1300		2 h at 1300 °C and fast cooling
	TN 1300/650		2 h at 1300 °C, 10 h at 650 °C and fast cooling
	TN WQ		10 min at 1300 °C and water quenching
	TN fast cooled	~75 K/min	
Ti-22Nb-10Zr	TNZ	10 K/min	
	TNZ 1300		2 h at 1300 °C and fast cooling
	TNZ 1300/650		2 h at 1300 °C, 10 h at 650 °C and fast cooling
	TNZ WQ		10 min at 1300 °C and water quenching
	TNZ fast cooled	~75 K/min	
Ti-22Nb-10Zr-0.3B	TNZ3B	10 K/min	
	TNZ3B 1300		2 h at 1300 °C and fast cooling
	TNZ3B 1300/650		2 h at 1300 °C, 10 h at 650 °C and fast cooling
	TNZ3B WQ		10 min at 1300 °C and water quenching
	TNZ3B fast cooled	~75 K/min	
Ti-22Nb-10Zr-0.5B	TNZ5B	10 K/min	
	TNZ5B 1300		2 h at 1300 °C and fast cooling
	TNZ5B 1300/650		2 h at 1300 °C, 10 h at 650 °C and fast cooling
	TNZ5B WQ		10 min at 1300 °C and water quenching
	TNZ5B fast cooled	~75 K/min	

Material	Sample name	Cooling after sintering	Heat treatment
Ti-22Nb	TN XRD	10 K/min	
	TN XRD 1300		2 h at 1300 °C and fast cooling
	TN XRD 1300/650		2 h at 1300 °C, 10 h at 650 °C and fast cooling
	TN XRD WQ		10 min at 1300 °C and water quenching
Ti-22Nb-10Zr	TNZ XRD	10 K/min	
	TNZ XRD 1300		2 h at 1300 °C and fast cooling
	TNZ XRD 1300/650		2 h at 1300 °C, 10 h at 650 °C and fast cooling
	TNZ XRD WQ		10 min at 1300 °C and water quenching

Appendix II – Optical micrographs of TNZ5B

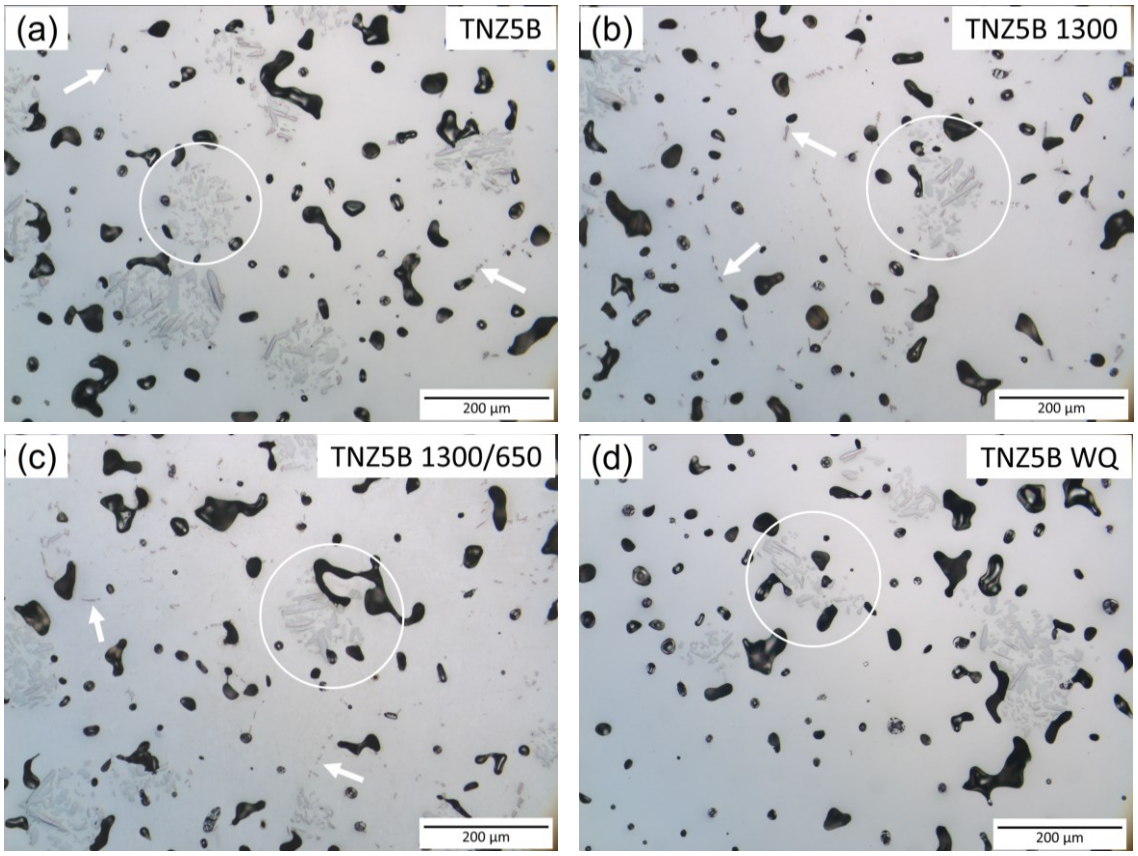

App. Figure 1: Optical micrographs of (a) TNZ5B, (b) TNZ5B 1300, (c) TNZ5B 1300/650 and (d) TNZ5B WQ. Carbides are indicated by arrows. Boride islands are indicated by circles.

Appendix III – BSE-images of TNZxB

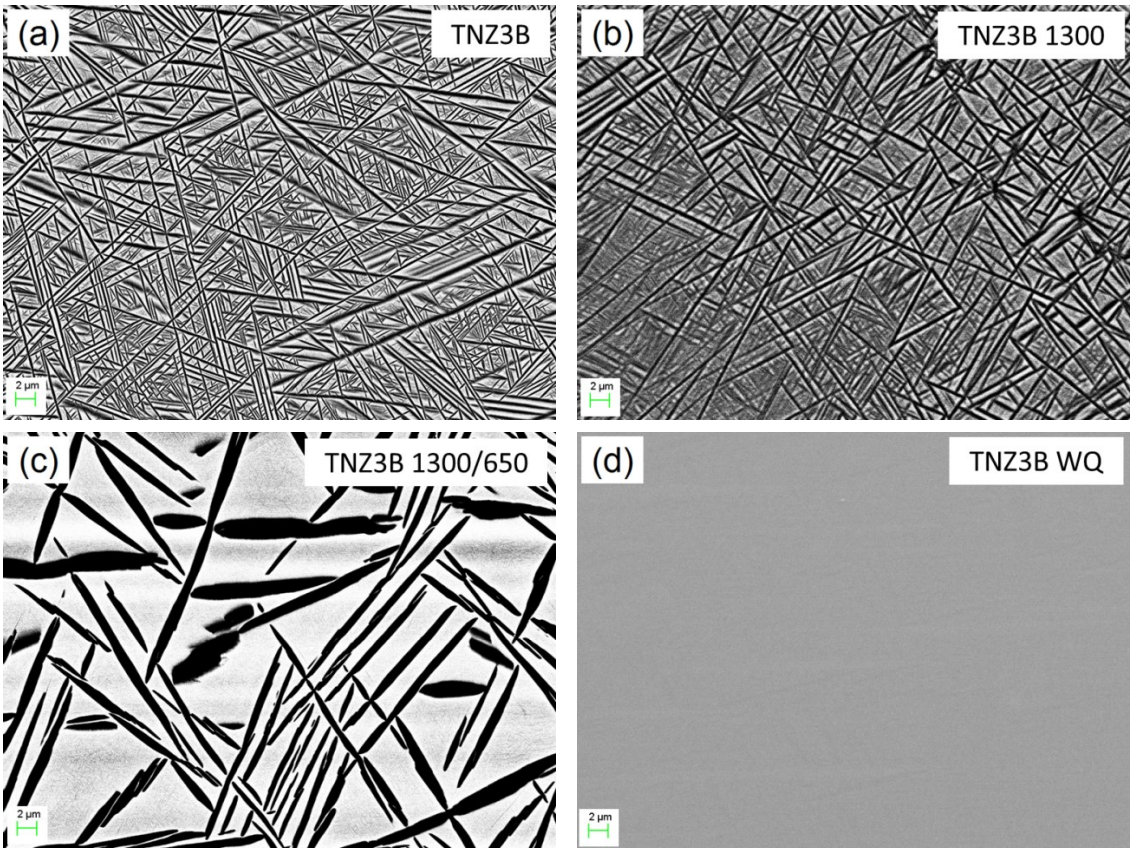

App. Figure 2: BSE-images of (a) TNZ3B, (b) TNZ3B 1300, (c) TNZ3B 1300/650 and (d) TNZ3B WQ

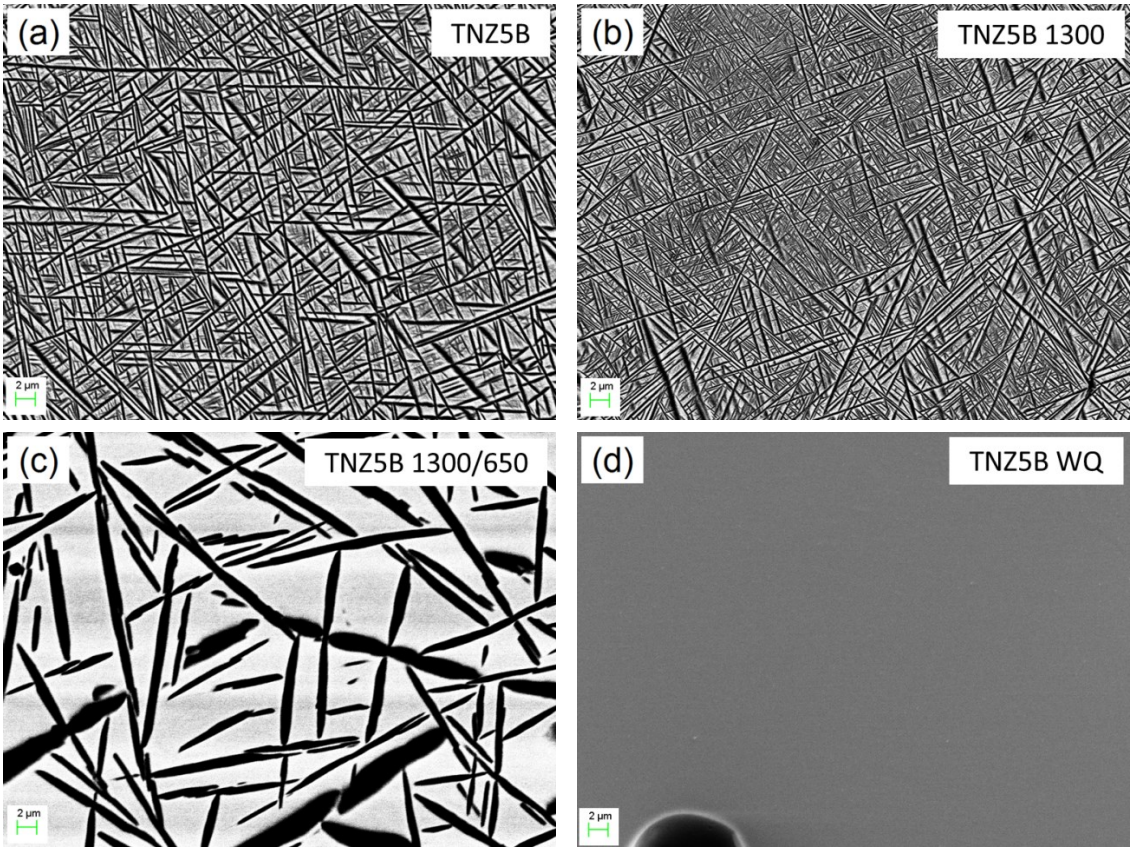

App. Figure 3: BSE-images of (a) TNZ5B, (b) TNZ5B 1300, (c) TNZ5B 1300/650 and (d) TNZ5B WQ

Appendix IV – EDS analysis of TNZ and TNZxB

App. Table 2: EDS analysis of TNZ standard sintered and after heat treatments in at.%

(a) TNZ

	α-β structure	α	β	Carbide
Ti	78.9	81.3	77.2	61.3
Nb	13.5	11.9	14.9	2.7
Zr	7.5	6.9	8.0	5.0
C	n/a	n/a	n/a	31.1

(b) TNZ 1300

	α-β structure	α	β	Carbide
Ti	78.9	80.7	42.4	59.5
Nb	13.7	12.2	14.7	2.9
Zr	7.5	7.2	8.0	5.2
C	n/a	n/a	n/a	32.4

(c) TNZ 1300/650

	α-β structure	α	β	Carbide
Ti	78.8	90.5	76.9	62.8
Nb	13.6	4.1	15.3	3.1
Zr	7.6	5.3	7.8	5.1
C	n/a	n/a	n/a	29.0

(d) TNZ WQ

	α-β structure
Ti	79.9
Nb	12.5
Zr	7.5
C	n/a

App. Table 3: EDS analysis of TNZ3B standard sintered and after heat treatments in at.%

(a) TNZ3B

	α-β structure	α	β	Carbide
Ti	79.6	80.1	79.2	59.2
Nb	12.9	12.6	13.2	2.6
Zr	7.5	7.2	7.6	7.2
C	n/a	n/a	n/a	31.0

(b) TNZ3B 1300

	α-β structure	α	β	Carbide
Ti	79.2	79.6	79.6	59.1
Nb	13.0	12.7	12.7	3.3
Zr	7.8	7.7	7.6	6.6
C	n/a	n/a	n/a	31.0

(c) TNZ3B 1300/650

	α-β structure	α	β	Carbide
Ti	79.6	48.0	75.3	58.1
Nb	12.7	5.7	16.6	2.7
Zr	7.7	6.3	8.2	6.0
C	n/a	n/a	n/a	33.3

(d) TNZ3B WQ

	α-β structure
Ti	78.8
Nb	13.5
Zr	7.7
C	n/a

App. Table 4: EDS analysis of TNZ5B standard sintered and after heat treatments in at.%

(a) TNZ5B

	α-β structure	α	β	Carbide
Ti	78.9	80.1	43.1	56.1
Nb	13.2	12.4	13.9	2.4
Zr	7.9	7.5	8.1	7.9
C	n/a	n/a	n/a	33.6

(b) TNZ5B 1300

	α-β structure	α	β	Carbide
Ti	8.0	799.2	78.4	59.5
Nb	13.4	13.3	13.8	3.0
Zr	7.6	7.5	7.8	5.8
C	n/a	n/a	n/a	31.7

(c) TNZ5B 1300/650

	α-β structure	α	β	Carbide
Ti	79.2	85.8	75.1	61.7
Nb	13.1	7.7	16.9	3.7
Zr	7.7	6.5	8.0	4.9
C	n/a	n/a	n/a	29.7

(d) TNZ5B WQ

	α-β structure
Ti	78.8
Nb	13.8
Zr	7.5
C	n/a